DISCLAIMER NOTICE

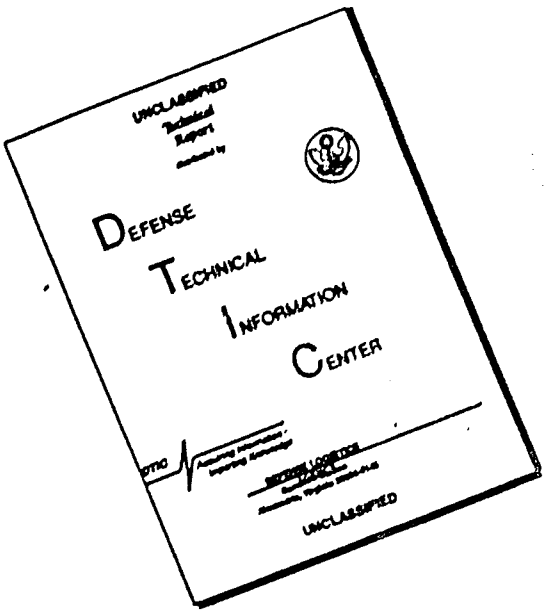

THIS DOCUMENT IS BEST QUALITY AVAILABLE. THE COPY FURNISHED TO DTIC CONTAINED A SIGNIFICANT NUMBER OF PAGES WHICH DO NOT REPRODUCE LEGIBLY.

CALIFORNIA INSTITUTE OF TECHNOLOGY

Hydrodynamics and Mechanical Engineering Laboratories

TIP CLEARANCE FLOWS IN AXIAL FLOW COMPRESSORS AND PUMPS

by

Dean A. Rains

REPORT NO. 5

JUNE, 1954

Under Navy Contracts N6-ori-102 Task Order IV and Nord 9612

TIP CLEARANCE FLOWS IN AXIAL FLOW COMPRESSORS AND PUMPS

Under Navy Contracts N6-ori-102 Task Order IV

and Nord 9612

Prepared by:

Dean A. Rains

Approved by:

W. D. Rannie
Associate Professor of
Mechanical Engineering

A. J. Acosta
Senior Research Engineer,
Hydrodynamics Laboratory

Hydrodynamics and Mechanical Engineering
Laboratories

California Institute of Technology
Pasadena, California
June 1954

ACKNOWLEDGMENTS

The author wishes to acknowledge the helpful guidance of Drs. W. D. Rannie and A. J. Acosta while conducting this research. A Daniel and Florence Guggenheim Foundation Fellowship in Jet Propulsion afforded financial assistance to the author.

The efforts and cooperation of Messrs. T. W. Fuller, J. R. Kingan, E. F. Daly, G. M. Hotz and many others made the construction of the axial flow pump facility possible.

Miss Zora Lindberg, Mr. J. C. Ribbons, Mr. F. T. Linton and Miss Mildred Olson put the report in its final form.

TABLE OF CONTENTS

Acknowledgments		i
Abstract		ii
Table of Contents		iii
Summary		v
I.	Introduction	1
II.	Equipment and Experimental Techniques	3
	A. Introduction	3
	B. Pump and Pump Circuit	5
	C. Instrumentation	8
	D. Blade Construction	9
	E. Flow Visualization	11
	F. Blading Design	14
III.	Flow Within the Tip Clearance and Losses	17
	A. Introduction	17
	B. Preliminary Discussion of the Tip Clearance Flow Model	18
	C. Modifications to the Perfect Fluid Model Due to Real Fluid Effects in a Turbomachine	20
	D. Two Dimensional Potential Flow in a Clearance Space	21
	E. The Calculation of the Laminar Flow in the Clearance Space for a Stationary Blade	26
	F. The Calculation of the Tip Clearance Velocity for a Stationary Blade with Both Inertia and Friction Forces Included	31
	G. The Effect of Blade Rotation on the Tip Clearance Flow	32
	H. The Calculation of the Tip Clearance Velocity with Rotational Effects Included	36

I. Tip Clearance Flow Losses 39

IV. Flow Outside the Tip Clearance 46

A. Introduction 46

B. Observations of Tip Vortex Cavitation in Axial Flow Pumps 46

C. Discussion of the Cavitation Experiments 50

D. Observations on the Formation of a Vortex Due to a Thin Jet Entering a Stream 52

E. The Formation of the Vortex Sheet Due to a Jet Entering a Stream and Its Roll Up Into a Vortex 53

F. Formation of the Vortex Sheet Near a Blade Tip with Its Subsequent Rolling Up 56

G. The Estimation of the Inception of Cavitation 61

References 66

Appendix A - Notation 68

Appendix B - Calculation of $K = \frac{P_\infty - P_v}{\frac{1}{2}\rho W_\infty^2}$ and Angles of Attack 72

Figures 73

SUMMARY

The influence of the clearance between the rotor blade tips and the duct wall on efficiency of compressors has been the subject of several investigations in the past. The results, as given in scattered reports of experiments, have indicated that appreciable gains in efficiency could be made by reducing tip clearances below currently accepted values. In spite of such experimental evidence, the importance of tip clearance losses does not seem to have been sufficiently emphasized. The principal reason for this is that experiments have been confined to overall efficiency measurements on compressors and the tip clearance flows themselves have not been studied. The lack of knowledge of the mechanism by which the clearances introduced losses raised some doubts concerning the validity of interpretation of the overall efficiency measurements.

Several more or less elaborate theoretical investigations of tip clearance flows have been made in the past based on the lifting line concept of a wing with a gap. Induced drag has been determined from these theories and attempts made to interpret these in terms of tip clearance losses. That these attempts have not been successful in explaining the experimental efficiency measurements is not surprising, because of the obvious inadequacy of the model. The clearance dimension in practice is a few percent of the chord, or even a few percent of blade thickness at most, so it is very unlikely that a lifting line assumption could apply. Some very crude methods of estimating losses from tip clearance flow have been based on the assumption that a leakage flow, resulting from the

pressure difference over the rotor, occurs in an annulus of height equal to the clearance height. This model, which would be reasonable if the number of blades were infinite, is probably more realistic than the lifting line theories even for a finite number of blades.

The purpose of this investigation was to find out the nature of the tip clearance flow and to devise an appropriate model so clearance losses could be calculated in a rational manner. Since direct measurements of the flow field in the region of the clearances were almost impossible, an essential first step was to make the stream lines visible so the general character of tip clearance flow could be determined. Air is not a very satisfactory medium for observations of this kind because very small particles introduced into the air stream diffuse too rapidly in turbulent flow for good visibility. Hence a pump with blading similar to a compressor was used and observations made with water as a medium by introducing droplets of colored oil of a specific gravity of unity into the flow. The drops need not be as small as the particle size required to follow closely the stream lines in air. A further advantage of water as a medium is that the system pressure can be lowered to cause cavitation. If vortices occur in the flow, cavitation occurs in the regions of low pressure in the vortex cores and makes them clearly visible. This latter effect was found very useful. Several auxiliary experiments were made in water tunnels and flumes in order to isolate certain effects that were difficult to observe in the pump.

The most important result of the investigation is a simple perfect fluid model of tip clearance flow from which estimations of losses can be

made easily. The essential character of the model is best imagined as a wing with a narrow slot where the plane of symmetry through the slot represents the wall at the end of a blade. Because of the pressure difference over the wing, a narrow jet issues from the slot at the suction surface. The pressure in the jet is the same as the pressure in the fluid outside the jet, so the magnitude of the velocity at any point in the jet must be the same as the local velocity outside the jet, a result of the application of Bernoulli's equation. However the chordwise component of the velocity in the jet is the same as the velocity on the pressure surface of the wing, since the fluid in the jet came from that region and hence is less than the velocity outside the jet. The component of velocity normal to the chord in the jet is a result of conversion of the pressure difference over the wing into kinetic energy.

The velocity in the jet is inclined at an angle to the free stream direction and the sides of the jet consist of vortex sheets in which the vortex lines must be in the direction of the vector mean of the velocities inside and outside the jet. Since the vortex sheets are close together and the vortex lines are inclined at an angle from the chord line, the induced velocity from a pair of vortex lines in the sheets can have a local effect only. The induced velocities must die out rapidly in both chordwise and spanwise directions. Hence the problem of determining flow distribution is considerably simpler than for the somewhat analogous problem of vorticity shed from the edge of a wing of low aspect ratio where the influence of the shed vorticity is not so localized.

Observations show that the shed vortex sheet rolls up rapidly into a tight vortex along its leading edge. However, the influence of this rolling up is probably quite localized also and does not affect the distribution of clearance flow. A simple calculation of the strength of the vortex sheet from the model shows that the entire circulation about the wing appears in the vortex sheet and the distribution is the same in proportion as the chordwise distribution for the wing. Hence there is no vorticity shed from the wing trailing edge in this model: the Kutta condition has been satisfied at the edges of the slot rather than at the wing trailing edge.

Viscous effects complicate the actual flow as compared with this model, but their influence on the more important aspects of the flow is surprisingly small. The frictional resistance to flow through the tip clearance was found to be small for the dimensions that are ordinarily mechanically feasible. The rolling up of the vortex sheet is more rapid and of somewhat different character when there is no relative motion between the blade and the wall as compared with the case of relative motion as in a turbomachine. This indicates that viscous forces have a strong effect on the rolling up process. Further complications arise in the turbomachine from the scraping of the rotor tip through the wall boundary layer. This seems to produce an additional pressure on the under surface of the blade which appreciably increases the tip clearance flow rate.

The perfect fluid model by itself does not give any losses in the sense of dissipation of energy. However, a plausible assumption is that

the kinetic energy of the velocity component in the clearance normal to the chord and hence to the free stream flow cannot be recovered. The observation that the vortex sheet rolls up is evidence that this kinetic energy quickly appears in a type of motion where dissipation must occur rapidly. On this basis, losses for various values of tip clearance were calculated and compared with the results of overall efficiency measurements in the pump and with other measurements in a compressor where the blade design had been given in sufficient detail. The results of the comparison were very satisfactory; hence the principal purpose of the investigation was accomplished.

Some refinements of the idealized model were made to account for the influence of the viscous resistance on the clearance flow rate and to account for the increased pressure on the lower surface of the blade resulting from the impact of the wall boundary layer. In addition a calculation of the limiting case of extremely small tip clearance, where viscous effects are predominant, is given.

The rolling up of the tip vortex sheet does not appear to change the magnitude of the losses, and hence its rate of rolling up is not particularly significant in the overall flow characteristics of a compressor. In the pump, however, it was shown that cavitation occurs first in the rolled up tip vortex before cavitation can be observed on the blade surface. This early cavitation away from surfaces does not in itself affect performance and is unlikely to cause damage. However the prediction of the vortex cavitation and its alleviation is of some interest. An attempt was made to develop a theory for the rate of rolling up of the vortex

sheet and to estimate its strength so incipient cavitation could be predicted. Unfortunately the influence of real fluid effects cannot be taken into account in a simple manner; hence the theory is not as complete or as satisfactory as desired.

I. INTRODUCTION

As turbomachinery has developed in the past twenty years, designers have continued their efforts to build more dependable highly efficient light weight machines with a wide range of stable operation. More and more information on elasticity, vibration dynamics, metallurgy, heat transfer, and fluid mechanics has been required to pursue this development. Considerable success has been achieved in work toward these goals, but in particular the high efficiency of modern machines has been realized without a complete understanding of the loss mechanisms in the various components of the machine. High efficiency of each component is especially important in a gas turbine, since the over-all performance of the engine is very dependent on the good performance of each component. This statement is born out by Figure 1 which shows the change of thermodynamic cycle efficiency with changes in turbine and compressor performance [1]. The compressor is so important because it uses roughly two-thirds of the turbine output. A gas turbine in this respect is quite different from a steam turbine plant where the power required for the boiler-feed pumps is an insignificant portion of the turbine output. This is one of the primary reasons that steam turbines were developed long before gas turbines.

A great deal of effort has been expended in the last eight years to understand the factors that determine compressor performance. The state of ignorance is expressed in a recent summary by Chung-Hua Wu in Reference 2 and is well summarized in Figure 2 taken from Reference 3.

At the design point the losses are broken down approximately as 2.2 percent due to annulus loss, 4.4 percent due to "secondary" loss, and 4.2 percent due to profile losses. The annulus and blade profile losses can be explained by their similarity to pipe flow loss and single airfoil implication is that it is caused by flow other than the primary flow through the machine. These secondary flows may be classified as follows:

(1) The cross flows in the boundary layers on the blades and annulus due to the turning of the flow.

(2) The cross flows in the boundary layers due to the rotation of the machine.

(3) Leakage flows through the tip clearances and the clearance space around shroud rings.

Research in the first two types of secondary flow has not yet accounted for the losses to be explained [4]. Various mechanisms have been suggested by which these types of secondary motion may be responsible for the losses [5], but at the present time the status of this phase of secondary flow research is inconclusive. The following is an attempt to gain a better understanding of the third type of secondary flow. Tip clearances will be studied particularly to evaluate them as a source of loss with the hope that another portion of the losses may be properly accounted for.

In the study of tip clearance flows information of specialized interest on the inception of cavitation in pumps is presented. For this investigation, however, the cavitation phenomena serve only as a means of studying tip clearance flows.

II. EQUIPMENT AND EXPERIMENTAL TECHNIQUES

A. Introduction

Most of the experimental research applicable to turbomachinery is done in machines with air as the working fluid. The use of air in the study of turbomachinery seems natural since they generally utilize an air cycle. Air is especially useful if the compressibility effects associated with high speed operation are important in the problems under study. There are advantages, however, in having slow speed air machines to do detailed experimental work without the excessive noise and stress problems that come with high rotative speeds. Some of the inherent advantages of air machines are that air is readily available, the sealing problems are few, and usually an expensive closed circuit is not required. The blading for such machines is still expensive, for rotor tip speeds of the order of 200 ft./sec. or more are required to give desirable Reynolds numbers of the order of 100,000 based on mean axial velocity and blade chord. The cost of investigating various blade designs is very high under these conditions.

There are a number of advantages of having a water machine available for research work, the most apparent of which is that under atmospheric conditions the kinematic viscosity of air is thirteen times larger than water [6]. Thus for the same Reynolds number a water machine may be designed for greatly reduced speeds, size, power consumption, and blade stresses as compared to an air machine. With the low strength requirements at the reduced rotational speed, a research machine can use lead-alloy blades. The cost of these blades may be

reduced to such a level that numerous changes in the stage blade design are not prohibited.

In order to obtain the magnitude of the savings possible by using a water machine instead of an air machine, scaling ratios will be considered for retention of the Reynolds number based on the blade chord and mean axial velocity as a fixed parameter. For complete geometric scaling the rotative speed (U_o) and machine diameter (D) are related by

$$\frac{D_w}{D_a} \quad \frac{U_{ow}}{U_{oa}} = \frac{\nu_w}{\nu_a} \tag{1}$$

The power requirement (P) is scaled by

$$\frac{P_w}{P_a} = \frac{\rho_w}{\rho_a} \quad \frac{\nu_w^2}{\nu_a^2} \quad \frac{U_{ow}}{U_{oa}} \tag{2}$$

Thus by the choice of one of the three available ratios the other two are determined by (1) and (2). The results for a choice of unity for each ratio are shown in the table below.

D_w/D_a	U_{ow}/U_{oa}	P_w/P_a
1.00	0.08	0.39
0.08	1.00	5.00
0.39	0.20	1.00

The primary difficulty of scaling down a machine completely is that the blades become so small that it is difficult to make them and still retain the original thickness distribution. One method of alleviating this construction problem is to decrease the number of blades while keeping the solidity (the blade chord to spacing ratio) constant. The aspect ratio of the blades is changed with this scaling procedure, so new relations must be written

$$\frac{D_w}{D_a} \quad \frac{U_{ow}}{U_{oa}} = \frac{\nu_w}{\nu_a} \quad \frac{N_w}{N_a} \tag{3}$$

and

$$\frac{P_w}{P_a} = \frac{\rho_w}{\rho_a} \frac{\nu_w^2}{\nu_a^2} \frac{N_w^2}{N_a^2} \frac{u_{ow}}{u_{oa}} \qquad (4)$$

Another arbitrary ratio has been introduced in the scaling proportionality relations which permits an even wider choice of designs. In the table below the ratios are computed for the same given ratios as in the previous table except that $\frac{N_w}{N_a} = 0.50$.

D_w/D_a	u_{ow}/u_{oa}	P_w/P_a
1.00	0.04	0.05
0.04	1.00	1.25
0.05	0.80	1.00

During 1952 an axial flow pump test facility was constructed in the Hydrodynamics Laboratory to utilize these advantages and others that will be discussed in the section on flow visualization techniques (II-E).

B. Pump and Pump Circuit

A machine was desired for internal flow studies, performance investigations, and cavitation experiments. These requirements led to the design of a vertically mounted test unit installed in a simple closed hydraulic circuit using water as the working fluid. The rotor is externally driven by a D.C. dynamometer which provides the only power for flow circulation.

The circuit itself (see Figures 3 and 4) consists of the test pump which discharges into a vaned elbow and thence into a diffuser section. Another vaned elbow directs the flow downward through a second diffuser and hence into a "lattice" type throttling device. The circuit is closed through two more vaned elbows and a 6:1 contraction

nozzle. The circuit is fabricated from 1/4 inch galvanized plate.

The test unit and dynamometer are mounted separately on rigid steel bases grouted to a concrete wall.

An advantage of having a closed circuit is that the system pressure level may be readily controlled. Auxiliary pressurizing and evacuating circuits are provided so that the ambient pressure in the unit can be arbitrarily fixed between 25 psi and 26 inches of Hg vacuum.

The test unit is approximately forty inches long, fourteen inch inside diameter, and can accommodate up to three stages of blading. The general design features are shown in Figure 5. The pump unit is vertically mounted and split longitudinally in halves. One half of the pump case is bolted and doweled to the mounting plate, while the other half is removable by a roll-away jig-assembly which is permanently attached to the structure. The same jig may be used for the removal of the rotor assembly. The removable case-half contains a lucite viewing window which runs the full length of the rotor and extends circumferentially over two blade passages. Flow surveying ports are also incorporated in the removable case-half behind each of the four stationary blade row positions, as well as a single surveying hole behind each of the rotor blade row positions. Static pressure taps are located in the fixed casing-half between each blade row.

The stationary blades, i.e., the entrance, stator, and exit blades, are attached to two-inch wide circular segments which are fastened into grooves machined in the case. There are eighteen stationary blades per row and sixteen rotor blades per row. The rotor blades

are attached by means of segments in the same manner as the stator blades.

A survey plate is provided immediately downstream of the contraction nozzle so that the flow distribution entering the test unit can be determined.

Both the rotor and the case are cast of red brass. All of the shafting is stainless steel. The drive shaft is hollow to permit communication with the rotor while the machine is rotating. The advantage of this feature will be described in the section on flow visualization (II-E).

The test unit may be disassembled and the rotor removed in about three man-hours. However, access to the rotor blades is possible in less time by removing the window.

The dynamometer used to drive the pump is mounted vertically about three feet above the first elbow. Space is thus available for attaching equipment that must rotate with the machine, such as a manometer to measure pressures in a rotating reference frame.

The motor is rated at 30 hp at 1750 rpm on 230 volt D.C. The power is supplied by a 30 KW thyratron rectifier unit. A differential gear box is used to establish the rotative speed in unit rpm increments above about 100 rpm. With this controller speed regulation is maintained on the average to within one part in ten thousand.

A torque arm and pan weight system is used to measure the torque reaction. An electrical displacement pickup gives the location of the arm between stops 0.004 inches apart. The signal from the pickup is used as a null indicator, so that the arm is returned to its original balance position

for each reading. The sensitivity of the torque measuring equipment is about 0.25 inch-pounds.

C. Instrumentation

The measurements of torque and speed have already been described. The other overall flow quantities which must be determined are flow rate, head increase across the pump, and the system pressure. The pressure drop across the contraction nozzle upstream of the pump provides a convenient measure for the determination of the system flow rate. The nozzle was calibrated from velocity surveys taken at its exit. In order to determine the head rise, total head rakes, each with nine probes, are set flush and faired into the leading edges of each of the three legs of the downstream bearing support. The pressure differences between these probes and a total head probe in the center of the nozzle exit survey plate are read on a multi-tube manometer bank. A water-mercury manometer is used to measure the pressure level in the circuit.

More detailed flow measurements can be made through the surveying ports in the casing. Each of the ports, or slots, behind the stationary blade rows extends circumferentially over approximately two blade passages. To avoid the sealing problems of a more elaborate traversing device, the probes are located through a plug which permits no smaller than 2° increments in circumferential surveys. A special probe holder was built to position all of the probes radially within 0.01 inch and circumferentially within 0.25° respectfully. The probe holder, probe, and plug assembly are shown in Figure 6 ready for installation in

the machine. The probe holder can also be mounted in the surveying station behind each of the rotor blade rows. An assortment of various types of probing instruments has been made, a few of which are shown in Figure 7. From left to right they are: a static pressure probe, a claw-type directional probe, a boundary layer total head probe, and a Kiel-type total head probe. Calibration of the direction and static pressure probes was checked from time to time in the air jet discharge of a large contraction nozzle.

The measurement of the pressures from these various probes was made with a Statham liquid differential pressure gage of total range 1 psi and a Baldwin-Southwark strain gage bridge. The gage was calibrated frequently with an air-water manometer. With the use of this transducer, pressures can be measured to 1/1000 of the full scale reading. A Statham gage is ideal for use with the claw probe since no flow is required for a null reading. Flow angles can be measured to within $\pm$ 0.25^{o} by this technique.

In order to determine the rotor blade tip clearances as installed in the machine, four holes are provided in the case at each rotor row position for depth micrometer measurements.

D. Blade Construction

As it has been pointed out, the use of water as the working fluid allows the rotative speeds to be in the 200-300 rpm range and still have Reynolds numbers of 80,000 to 120,000. At these low speeds the centrifugal stresses in the blades are negligible, and the hydrodynamic bending

stresses are less than 500 psi. Strength, therefore, is practically ruled out as a problem in selecting the material for blade manufacture. To minimize the costs of manufacturing the blades were to be cast in the Hydrodynamics Laboratory, so low melting point alloys (300° - 400°F) were desirable. The low melting point eliminated the need of any special furnace and handling equipment. "Cerro-base" and "Cerro-cast", lead-bismuth alloys, were chosen since they met the minimum strength requirements and were commercially available. The lead was selected instead of a plastic because of its superior dimensional stability and casting ease.

The blades were cast centrifugally in two-piece reusable plaster molds. The blades were cast onto the brass holding segment in order to simplify the attachment problems. The mold halves were formed on an accurately machined brass master blade. One master blade was provided for each of the four types of blades in the machine, i.e., pre-rotation vanes, rotor, stator, and rear straightening vanes. The master blades were made by first spotting coordinate points on a brass block with a milling machine and completed by hand finishing to these points. The casting procedure consisted of heating the mold and then forcing the molten metal centrifugally into the mold by using the arrangement shown in Figure 8. After fabrication a few blades were selected at random for inspection. It was found that the chords were within 0.2 percent of their design values, and the stagger angles at the tip were within 0.1° of the design angle.

The outside diameter of the rotor blades and the inside diameter

of the stationary blades were trimmed by machining a complete blade row in a jig to give the desired running tip clearances. More details of the blade construction are given in Reference 7.

As interest in tip clearance flows developed, information on the cavitation performance of axial flow pumps was required. The blades that have been described are not sufficiently strong to operate at the 600 rpm required for the cavitation studies. Hence, beryllium copper replicas of the first blade set were cast commercially. All of these blades were cast with a "foot" that was held in the slotted segments by four screws. The tip clearance of the rotor blades was made variable by deepening the root slot and adding shims, thus permitting clearances from 0.004 inches to 0.100 inches. (See Figure 9)

E. Flow Visualization

Where very complicated flows occur and difficulty in interpretation of direct measurements is anticipated, means of observing actual stream lines is frequently of great value in preliminary studies. In order to do this, visible particles must be introduced into the flow so that they follow the stream lines closely without changing the flow pattern appreciably. Such particles must be very small if their density is different from that of the fluid so inertia effects are suppressed, or if the particles are large, their density must be the same as that of the fluid and they should be introduced into the fluid with velocities close to that of the fluid at the point of introduction. In laminar flow, very small particles are probably more satisfactory [8], but in turbulent flow the concentration of

particles dies out very quickly downstream of the point where they are introduced. Since it is the concentration of small particles that is visible rather than the individual particles, the use of small particles is not satisfactory in turbulent flow. Larger particles, however, can be followed individually in turbulent flow as far downstream as one wishes. The turbulent diffusion of large particles will of course be the same as for small particles. Since individual large particles are followed, the statistical distribution of the paths of many will give the required information on mean stream lines.

It is clear that large particles of solid or liquid cannot be used with air because of their inertia effects, so observations on air flow must be confined to low Reynolds numbers. However, water serves as an ideal transporting medium for immiscible colored oil tracers. The oil droplets remain of appreciable size due to the influence of surface tension and can be observed easily, so that flows with Reynolds numbers of the order of 100,000 or more may be examined. The tracer fluid that was found most successful for this work was a combination of di-butyl phthalate and kerosene mixed to give neutral buoyancy. Of course, the lucite window which extends the full length of the test installation was essential for this work.

The use of the flow visualization technique made possible the study of some of the three-dimensional flows in the machine, and hence served as the foundation of this investigation. It is difficult to get quantitative information on flow quantities by visualization techniques, but the flow geometry can be recorded for study and analysis.

To illustrate the technique, two examples of its use in the machine will be described in some detail.

Ordinarily in a curved channel the end wall boundary layer flow overturns and travels up along the convex side of the bend [9]. If the end wall is moving with respect to the channel walls, as is the situation at the rotor blade tips of an axial flow machine, will the flow still overturn? The visualization method will be used to answer this question.

A small brass injector tube was attached to the rotor of the pump. This injector was connected with tubing by way of the hollow shaft to a vessel rotating on the shaft of the machine. From this vessel dyed oil was forced under pressure into the flow. The volume flow rate was adjusted so that the jet of oil entered the flow at approximately the same velocity as the surrounding flow. The flow could then be observed through the window by using a stroboscopic light synchronized with the shaft rotation. The photographs shown in Figures 10, 11, and 13 were taken with a four by five inch view camera with lighting supplied by single flash lamps synchronized with the machine's rotation.

A comparison of the flow angles in the two photographs of Figure 10 shows that the flow is underturned near the outside case. In this figure and in Figure 11, δ is the thickness of the outside wall boundary layer, and y is the distance of the injection point from the wall. The conclusion is that the retarding drag on the flow by the case wall actually cancels out the overturning cross flow and turns the flow toward the blade surface leading in the rotation. Part of this "scraping" flow eventually impinges on the pressure side of the blade with a weak vortex being formed as a

consequence [8]. Some quantitative information can be obtained by measuring the flow angles in the photographs.

The flow visualization technique described in the previous paragraphs was also used to study the secondary flows near the rotating hub. The importance of boundary layer cross flows has often been discussed and measured with directional probes, but this photographic technique serves as another method to judge their importance. Figure 11 shows that the strong cross flows are limited to the bottom fifteen percent of the boundary layer. It is interesting to note the fluid moving up along the blade surface in the bottom photograph ($y/\delta = 0.08$).

There are many other methods of applying the visualization method. A probe may be installed to study the flow in the stationary blades. Cavitation may serve as a visualization tool, since it occurs first in regions of lowest pressure in the flow, for instance in free vortices, (See Figure 29). Flow visualization experiments were also carried out in simpler configurations representing certain aspects of the more complicated flow in the pump. A slow speed flume of one by four foot cross section in the Soil Conservation Laboratory was found useful in studying modeled flow geometries with oil droplets and dyed water injection.

F. Blading Design

For the first studies in the pump facility the blade design was chosen to be the same as in the compressor used for a research program in the Mechanical Engineering Laboratory [10]. The design point characteristics of these "free vortex" type blades are $\bar{\varphi} = \frac{\text{Mean Axial Velocity}}{\text{Tip Speed}}$

$= 0.45$ and $\overline{\psi}' = \dfrac{\text{Average Work Input}}{\text{Dynamic Pressure based on the Tip Speed}} = 0.40$. The fifty percent reaction point is at a radius ratio of 0.70 based on the outside radius. The ratio of the hub radius to the outside ratio (the hub ratio) is 0.60.

The number of blades for the pump was reduced from that in the compressor by the ratio 0.53 for constructional reasons after the diameter ratio had been set at 0.39. The resulting power ratio was 0.14 and the speed ratio was 0.10.

Since the rotor blades were of primary interest in the tip clearance flow study, a detailed tabulation of their design will be given here. There are sixteen rotor blades in the blade row. The blades have a parabolic camber line and a constant chord. The details of the rotor blade design are tabulated below as functions of the radial coordinate.

Radius Ratio $= R/R_o$	0.60	0.70	0.80	0.90	1.00
Solidity $= c/s$	1.15	0.985	0.860	0.765	0.690
Stagger Angle $= \beta^*$	15.2°	32.1°	43.8°	51.7°	57.4°
Camber Angle	46.7°	31.0°	20.3°	13.8°	9.8°
Maximum Thickness Ratio	0.12	0.11	0.10	0.09	0.08

The thickness function has an elliptically shaped nose and has its maximum thickness at the thirty-five percent chord position. The thickness function is tabulated below for a ten percent thick blade.

x/c	l/c	x/c	l/c
0.000	0.0000	0.300	0.0493
0.005	0.0085	0.350	0.0500
0.010	0.0122	0.400	0.0494
0.020	0.0167	0.450	0.0478
0.030	0.0208	0.500	0.0452
0.040	0.0232	0.550	0.0415
0.050	0.0254	0.600	0.0371
0.060	0.0277	0.650	0.0322
0.070	0.0297	0.700	0.0269
0.080	0.0315	0.750	0.0211
0.090	0.0331	0.800	0.0160
0.100	0.0346	0.850	0.0114
0.150	0.0404	0.900	0.0072
0.200	0.0446	0.950	0.0037
0.250	0.0474	1.000	0.0011

The thickness function for any other maximum thickness ratio may be obtained by simply scaling the values of l/c in the ratio of the maximum thicknesses.

The rotor blade chord is 1.90 inches and the installed rotor blade tip clearance is 0.007 inches.

Measurements of the overall pump performance showed that it gave a $\overline{\varphi} = 0.41$ at the design work coefficient ($\overline{\psi}' = 0.40$). Surveys of the flow angles from the entrance vanes, however, confirmed that they were accomplishing the flow turning for which they were designed. Surveys of the case and hub boundary layers downstream of the entrance vanes showed a layer with a displacement thickness of 0.071 inch on the case and a layer with a displacement thickness of 0.053 inch on the hub. Since the effective cross-sectional area of the machine is reduced thus by 4.6 percent, the mainstream portion of the blades is operating at a proportionally higher flow rate. This at least partially accounts for the discrepancy of eight percent between the designed and measured performance.

III. FLOW WITHIN THE TIP CLEARANCE AND LOSSES

A. Introduction

In Part I an approximate breakdown of compressor losses was considered in which the tip clearance losses were lumped with the unknown factors of "secondary" losses. However, experiments with fans, blowers, compressors, and turbines have shown appreciable drops in efficiency with increased tip clearance. If these results are extrapolated to zero clearance, the indication is that a good part of the unexplained losses are due to tip clearance flows.

More evidence of the importance of tip clearance flows was found by the visual observation of incipient cavitation in an axial flow pump [11]. The cavitation starts in the low pressure center of vortices created by the tip clearance flows.

Many designers have sought to minimize the tip clearance problem by incorporating shroud ring assemblies in their machines. The shroud ring joins all of the blade tips and thus eliminates the clearances. The ring is recessed in either the hub or case with or without labyrinth seals so there is still a leakage problem. Additional problems of alignment, stress, and rotational drag make the value of a shroud ring at the rotor blade tips doubtful. Many stator blade row assemblies have shroud rings where the lack of rotation and the smaller diameter make the ring more feasible.

The objectives of this investigation of tip clearance flows were (1) to understand the mechanism of the clearance flows and calculate their

magnitude, (2) to obtain a method of estimating the losses associated with the leakage flows, (3) to study the formation of the tip vortex with the purpose of finding methods to estimate its size and strength, and (4) to use the information found about the vortex to explain the incipient phase of cavitation in axial flow pumps.

B. Preliminary Discussion of the Tip Clearance Flow Model

For a perfect fluid the flow through a tip clearance must be the same as the flow through a slotted wing with the wall represented by the plane of symmetry through the slot. The flow through a slotted wing has been studied with the assumptions of the lifting line theory where the circulation is shed from the trailing edge as it drops to zero at the edges of the slot. Such a theory assumes that the width of the slot is large compared with the wing chord, an assumption that certainly does not apply to the tip clearance flow in a compressor where the slot width is more nearly of the order of one percent of the blade chord. Betz [12] has calculated the minimum induced drag and hence the maximum efficiency of a cascade of lifting lines with tip clearance, but of course his analysis is applicable only to fans where the tip clearance is large and the blade aspect ratio is high. Others have applied this or similar theories to the calculation of induced drag in compressors, but their validity is also dubious because of the lifting line assumption.

A much more reasonable model of the flow through a narrow slot in a wing is one where the Kutta condition is applied along the edges of the slot rather than at the trailing edge. Then the flow is more nearly analo-

gous to the flow around a wing of very small aspect ratio as considered by Bollay [13], because in both cases the vorticity is shed along the chord at the wing tip. However, the slotted wing is in some ways much simpler since the influence of the shed vorticity on the flow is confined to the immediate region of the slot. The effect of the vortex sheets dies out with distance more rapidly because of the nearby image in the plane of symmetry. Schematic diagrams of the vorticity shedding for a lifting line, a wing of low aspect ratio, and a wing with a narrow slot are given in Figure 12.

Direct observation of the flow by the various techniques already discussed has demonstrated that the model of the flow through a slot where the Kutta condition is satisfied along the edges of the slot is the best perfect fluid model of tip clearance flow.

Such a model, as described above, can be considered in various ways. The flow in the slot between the shed vortex sheets consists of a jet with uniform velocity across its width and in general varying velocity along the chord. If the free stream velocity for the wing is W_∞ and if P_1 and P_2 are the pressures on the pressure and suction sides of the wing away from the slot, then the velocity in the jet normal to the chord line is simply $W_t = \left\{\frac{2(P_1 - P_2)}{\rho}\right\}^{\frac{1}{2}}$ since the velocity in the jet parallel to the chord line is carried through without change for a wing of small thickness. This velocity component W_t is of the order of W_∞ for the usual blade loading in compressors since $\left\{\frac{2(P_1 - P_2)}{\rho W_\infty^2}\right\}^{\frac{1}{2}}$ is of the order of unity.

C. Modifications to the Perfect Fluid Model Due to Real Fluid Effects in a Turbomachine

A perfect flow model for the tip clearance flow problem has been outlined in the previous section. The question immediately arises, "How well is the flow in a machine represented by this model?" If the model does not adequately represent the flow in the machine, it follows naturally to ask, "What are the factors that require the model to be altered?", and "How can corrections to the model be made?"

In the small clearances that are characteristic of turbomachinery, the viscous forces must have an effect. However the small length to height ratio of a clearance (normally from five to twenty in a turbomachine) may exclude large viscous influences because the viscous forces have only a short length on which to act. Therefore, the importance and type of real fluid effects must be considered to obtain a correction to the perfect fluid model.

The viscous effects are manifested in three ways in the tip flow problem: (1) there is a resistance to the flow in the clearance, (2) the "no-slip" condition on the blade tip requires that fluid be pulled with the blade as it rotates, and (3) the case wall boundary layer flow impinges on the rotating blade (see Figure 10).

As a preliminary step in investigating the complete tip flow problem, a flow visualization experiment was conducted in the blade tip region. The results of the experiment are shown in Figure 13. An injector was placed at a distance of four times the tip clearance from the wall so that the oil would flow along the pressure side of the rotor blade. The

importance of the pressure difference across the blade may be seen by comparing the tip flows in the photographs for several pump flow rates. As the pump flow rate increases the blade pressure difference decreases, and therefore less fluid goes through the clearance. The tip flow appears to form a thin jet that streams out into the flow, maintaining its identity for a distance until it is rolled back by the main flow. After the jet is turned, it can be seen to become a part of a turbulent cone of flow. Although it cannot be discerned from these photographs, this cone will be shown in later experiments to be a vortex.

In a machine where the pressure side of the blade leads in the rotation (a pump or compressor) the viscous drag of the case wall moving relative to the blade tip also causes a flow relative to the blade tip from the pressure to the suction side. Therefore, this flow adds to the "pressure drop" leakage flow. In a turbine, where the suction side leads in the rotation, the leakage flow opposes the shear flow. The investigation presented herein will be restricted to pumps and compressors.

In compressors and pumps there are therefore two contributions to the tip flows: (1) the flow due to the pressure drop across the blade which may be primarily a perfect fluid phenomenon, and (2) the shear flow due to rotation which is a real fluid phenomenon.

D. Two Dimensional Potential Flow in a Clearance Space

If the viscous effects are neglected, a model of the tip clearance flows can be developed to show some of the primary characteristics of the flow. The next few sections are devoted to showing that the perfect fluid

effects do in fact dominate the real fluid effects in determining the clearance flow.

In general at stations along the chord of a blade, the pressure gradient across the blade is large compared to along the blade. Therefore as the flow is transported through the clearance, the velocity along the blade should be negligibly accelerated compared to the acceleration of the velocity normal to the blade. This is essentially the approximation made if sections normal to the chord are chosen to study the clearance velocity. For this two dimensional potential flow discussion the flow normal to the blade will be idealized as the free stream line flow into a slot. Figure 17 shows a comparison of the idealized geometry of the stream line separating from the inlet edge of the slot with the more plausible conditions of separation and reattachment at the inlet edge and the flow filling the clearance at the outlet. If the Bernoulli equation is applied to the condition far upstream and downstream in the tip flow,

$$W_t = \left\{\frac{2(P_1 - P_2)}{\rho}\right\}^{\frac{1}{2}} \tag{5}$$

or

$$\frac{W_t}{W_\infty} = (\Delta C_p)^{\frac{1}{2}} \tag{6}$$

which is the same answer obtained in III-B.

The validity of the perfect fluid model can be investigated by comparing measured pressure distribution near the tip with computed results. With the perfect fluid model the change in the pressure distribution on the pressure side of the blade is everywhere proportional to the square of the tip clearance velocity. However on the suction side of the blade, the jet of flow from the clearance should not materially affect the

pressure distribution because the stream lines are not appreciably curved. By using the hodograph method [14] of solving free stream line problems, the flow into a slot can be worked out readily to give

$$\chi = x + iy = \frac{\delta_t \sigma}{\pi} \left\{ \ln \frac{W_t + \varphi}{W_t - \varphi} - \frac{2W_t}{\varphi} + \frac{i\pi}{2} \right\} \qquad (7)$$

where σ, the contraction ratio, equals $\frac{\pi}{\pi+2}$ and φ is the complex velocity. This implicit relation for the velocities can be used with the Bernoulli equation to compute the pressures on the x and y axis. The results of these calculations are shown in Figure 21. The predominant feature of these results is the concentration of the pressure drop near the inlet of the clearance.

To compare the idealized flow model indicated in the previous paragraphs with experimental results, a stationary airfoil was chosen because the real fluid effects due to rotation would not be present. Of course there are boundary layers on the walls and blade, but boundary layers of thickness much less than the chord should not affect the pressure distribution on a blade with zero tip clearance. This picture is in sharp contrast to a two dimensional "strip theory" based on a lifting line that demands that the local lift is proportional to the local velocity squared. For applications to thin wall boundary layers, the Karman-Tsien lifting line theory [15] is thus quite inappropriate.

To carry out the pressure measurements, a two dimensional hydrofoil was installed normal to a wall containing a number of static pressure taps around the profile periphery. The taps were located on a disc set into the wall so that the taps could remain fixed relative to the

profile as the angle of attack was changed. The whole assembly was placed in an open channel water tunnel as shown in Figures 14 and 15. The Statham gage described in Section II-C was used to measure the static pressures on the wall. These experiments were run for a Reynolds number of 50,000 based on the free stream velocity and blade chord.

A typical set of data for several tip clearances is plotted on Figure 16. $\lambda = \frac{\text{Tip Clearance}}{\text{Maximum Blade Thickness}}$ was chosen as the tip clearance parameter because it characterizes the most important feature of the blade geometry for comparison of different blade shapes. The range of λ in turbomachinery practice is from 0.05 to 0.50.

From Figure 16 it is evident that for $\lambda > 0.100$ the strongest influence of the tip clearance on the wall pressures opposite the blade contour occurs on the pressure side of the blade. This is consistent with the above two dimensional flow model. In fact, a numerical comparison can be made between these two cases. Potential theory predicts a difference between the pressure at the inlet of the slot and the outlet of thirty-five percent of the pressure difference between far up and downstream (see Figure 21). The ratio measured at, for example, $\lambda = 0.167$ and $\frac{X}{C} = 0.4$ is $\frac{1.25 - 0.65}{1.25 + 0.35} = 0.375$. It is important to note that the pressure pattern does not change by doubling the clearance to $\lambda = 0.333$. Thus a potential flow pressure distribution is established for $\lambda > 0.167$. Therefore using a potential flow model in this range of tip clearances becomes more reasonable.

For $\lambda < 0.05$ the viscous forces become dominant and the pressure difference over the blade thickness is almost completely balanced by

the viscous resistance in the clearance. It is interesting to note that the lift is maintained up to the wall for zero tip clearances as was postulated above.

The Reynolds number for the flow in the clearance must be taken into account before any general inequalities can be written for the regimes of dominance of the viscous and inertia forces. To retain the same dimensionless pressure distribution from one Reynolds number to another, the ratio of the tip clearance velocity to the free stream velocity must also remain fixed. To obtain equal velocity ratios, the viscous pressure drop in the clearance must also be equal. For laminar flow, which probably will occur in the clearance because of the small clearance Reynolds numbers and the small length available for transition to turbulent flow, the dimensionless frictional pressure drop is $\frac{12\nu l}{W_\infty \delta_t^2}\left(\frac{W_t}{W_\infty}\right)$. Thus to keep the same pressure distribution $\frac{12\nu l}{W_\infty \delta_t^2}$ must be equal to a constant. More simply, $\lambda^2 R_l \epsilon$ must equal a constant, where R_l is the Reynolds number based on the free stream velocity and ϵ is the maximum thickness to chord ratio at the blade tip. Using the results of the pressure measurements on the wall, the viscous forces are predominant for $\lambda^2 R_l \epsilon < 11$ and the inertia forces are predominant for $\lambda^2 R_l \epsilon > 125$. It is important to note that for the large values of R_l typical of modern-day turbomachinery ($R_l > 250,000$) the viscous forces can be neglected for $\lambda > 0.07$, (ϵ is generally of the order of 0.10). Thus for the normally used clearances, the viscous forces can probably be neglected without large errors.

E. The Calculation of the Laminar Flow in the Clearance Space for a Stationary Blade

In the previous section it was shown that for $\lambda^2 R_1 \epsilon > 125$, two dimensional potential flow theory provides a reasonable model. More careful examination of the flow of a real fluid in the clearance is required to determine the importance of real fluid effects for smaller clearances. An example will be worked out to give the limiting case of tip clearance flows when the viscous forces dominate the inertia forces (i.e., acceleration terms may be neglected). The influence of the free stream flow around the blade is then equivalent to a given pressure distribution around the edges of the tip clearance. In order to simplify the calculation the clearance velocities across a two dimensional elliptically shaped airfoil at a small angle of attack will be computed.

As the first step in the analysis the pressure field around an elliptic cylinder must be determined. The flow that determines the pressure distribution can be considered as two dimensional potential flow hence making available the techniques of complex variables and conformal mapping.

In the physical (χ) plane, the elliptical cylinder has a geometry as shown in Figure 18. The flow from infinity is W_∞ with an angle of attack α . By using the well-known transformation [14]

$$\chi = \tau + \frac{c_o^2 - l_{m_o}^2}{16\,\tau} \qquad (8)$$

the ellipse is transformed to a circle of radius $\frac{c_o + l_{m_o}}{4}$ in τ plane. Thus the pressure distribution on the ellipse can be computed by evaluating

the velocity field in the τ plane with the Kutta condition applied at the point corresponding to the trailing edge in the χ plane, transforming the result to the χ plane and finally using the Bernoulli equation to give the pressure distribution.

This computation yields

$$C_p = 1 - \frac{4\{\sin^2\theta + 2\alpha \sin\theta(1-\cos\theta)\}}{1 - 2\left(\frac{C_o - l_{mo}}{C_o + l_{mo}}\right)\cos 2\theta + \left(\frac{C_o - l_{mo}}{C_o + l_{mo}}\right)^2} \qquad (9)$$

where $\cos\theta = \frac{2x}{C_o}$ and $\sin\theta = \frac{2y}{l_{mo}}$ if $\alpha \approx \sin\alpha \approx \tan\alpha$

To compute the flow through the clearance resulting from the above pressure distribution around the profile, all acceleration terms will be neglected. Taking the z axis along the blade span and neglecting the velocity in this direction, the equations of motion become

$$\frac{\partial p}{\partial x} = \mu\left(\frac{\partial^2 u}{\partial x^2} + \frac{\partial^2 u}{\partial y^2} + \frac{\partial^2 u}{\partial z^2}\right) \qquad (10)$$

$$\frac{\partial p}{\partial y} = \mu\left(\frac{\partial^2 v}{\partial x^2} + \frac{\partial^2 v}{\partial y^2} + \frac{\partial^2 v}{\partial z^2}\right) \qquad (11)$$

Assuming a parabolic variation of u and v in the z direction, the terms involving $\frac{\partial^2}{\partial z^2}$ may be eliminated from (10) and (11). Let

$$u = \bar{u}\left(\frac{6}{\delta_t^2}\right)\left(z\delta_t - z^2\right) \qquad (12)$$

and

$$v = \bar{v}\left(\frac{6}{\delta_t^2}\right)\left(z\delta_t - z^2\right) \qquad (13)$$

where δ_t is the tip clearance and $\bar{u}$ and $\bar{v}$ are mean velocities. Substituting these assumptions in (10) and (11) and integrating across the tip clearance gives

$$\frac{\partial p}{\partial x} = \mu\left(\frac{\partial^2 \bar{u}}{\partial x^2} + \frac{\partial^2 \bar{u}}{\partial y^2}\right) - 12\,\mu\,\frac{\bar{u}}{\delta_t^2} \tag{14}$$

$$\frac{\partial p}{\partial y} = \mu\left(\frac{\partial^2 \bar{v}}{\partial x^2} + \frac{\partial^2 \bar{v}}{\partial y^2}\right) - 12\,\mu\,\frac{\bar{v}}{\delta_t^2} \tag{15}$$

Under these assumptions the continuity equation remains

$$\frac{\partial u}{\partial x} + \frac{\partial v}{\partial y} = \frac{\partial \bar{u}}{\partial x} + \frac{\partial \bar{v}}{\partial y} = 0 \tag{16}$$

For very small clearances $\frac{\partial^2}{\partial x^2}$ and $\frac{\partial^2}{\partial y^2}$ are much smaller than $\frac{1}{\delta_t^2}$, so these terms are neglected from (14) and (15) to give

$$\frac{\partial C_p}{\partial x} = -\frac{24}{\delta_t^2}\left(\frac{\bar{u}}{W_\infty}\right)\left(\frac{C_0}{R_e}\right) \tag{17}$$

$$\frac{\partial C_p}{\partial y} = -\frac{24}{\delta_t^2}\left(\frac{\bar{v}}{W_\infty}\right)\left(\frac{C_0}{R_e}\right) \tag{18}$$

where $R_e = \frac{W_\infty C_0}{\nu}$

If (17) is operated on by $\frac{\partial}{\partial x}$ and (18) by $\frac{\partial}{\partial y}$ and the results added, it can be shown that $\nabla^2 C_p = 0$. Hence the methods of complex variables can be applied to find C_p and therefore $\bar{u}$ and $\bar{v}$ everywhere in the clearance. The problem can be greatly simplified if only the velocities on the boundaries are computed. The values of $\frac{\partial C_p}{\partial x}$ and $\frac{\partial C_p}{\partial y}$ on the boundaries alone are required to obtain this result.

In the circle plane coordinates, $\frac{\partial C_p}{\partial \theta}$ may be obtained by differentiation of Equation (9) giving

$$\frac{\partial C_p}{\partial \theta} = -\frac{2\alpha \sin^2\theta(1-\cos\theta)}{\left[\epsilon^2 + \sin^2\theta\right]^2} \tag{19}$$

if $\epsilon = \frac{l_{m_o}}{c_o}$ is small compared to one, so that terms of order ($\epsilon\alpha$) or (ϵ^2) may be neglected. If $\frac{\partial C_p}{\partial h}$ is also found on the profile, then $\frac{\partial C_p}{\partial x}$ and $\frac{\partial C_p}{\partial y}$ could be found by using the following relations between these derivatives

$$\frac{\partial C_p}{\partial \theta} = \frac{c_o}{2}\left\{\epsilon \cos\theta \frac{\partial C_p}{\partial y} - \sin\theta \frac{\partial C_p}{\partial x}\right\} \tag{20}$$

$$\frac{\partial C_p}{\partial h} = \frac{\epsilon \cos\theta \frac{\partial C_p}{\partial x} + \sin\theta \frac{\partial C_p}{\partial y}}{\left[\epsilon^2 + \sin^2\theta\right]^{\frac{1}{2}}} \tag{21}$$

The value of $\frac{\partial C_p}{\partial h}$ can be found readily by using the fact that it is the conjugate of $\frac{\partial C_p}{\partial \theta}$ on the circle in the τ plane. Potential theory [16] gives

$$\frac{\partial C_p}{\partial h} = P.V.\frac{1}{2\pi}\left(\frac{4}{c_o + l_{m_o}}\right)\int_{-\pi}^{\pi} \frac{\partial C_p}{\partial \gamma} \cot\left(\frac{\theta-\gamma}{2}\right) d\gamma \tag{22}$$

where P. V. stands for the principal value of the integral. The integral (22) was evaluated by using the method of contour integration with the result that

$$\frac{\partial C_p}{\partial h} = 8\alpha \frac{(1-2\epsilon)}{c_o \epsilon} \frac{\sin^2\theta(1-\cos\theta)}{\left[\epsilon^2 + \sin^2\theta\right]^2} \tag{23}$$

Therefore $\frac{\partial C_p}{\partial x}$ and $\frac{\partial C_p}{\partial y}$ were evaluated from (20) and (21) so that $\bar{u}$ and $\bar{v}$ are

$$\frac{\bar{u}}{W_\infty} = \frac{R_e}{6}\left(\frac{\delta_t}{c_o}\right)^2 \frac{\alpha \sin^6\theta}{\left[\epsilon^2 + \sin^2\theta\right]^3} \tag{24}$$

$$\frac{\bar{v}}{W_\infty} = \frac{R_e}{6}\left(\frac{\delta_t}{c_o}\right)^2 \frac{\alpha \sin^4\theta\left(\frac{1-\epsilon}{\epsilon}\right)(1-\cos\theta)}{\left[\epsilon^2 + \sin^2\theta\right]^3} \tag{25}$$

using Equations (17) and (18).

One deduction that can be made from these results is that the dominant term of $\frac{\bar{v}}{W_\infty}$ is of order unity, while $\frac{\bar{u}}{W_\infty}$ is of order α. This suggests that a two dimensional approximation can be made. If small strips perpendicular to the chord are considered and the local pressure gradient is approximated as local pressure difference across the blade divided by the blade thickness, $\frac{\bar{v}}{W_\infty}$ can be caluclated from

$$\frac{\Delta P}{l_o} = -12\,\mu\,\frac{\bar{v}}{\delta_t^2} \tag{26}$$

By using $l_o = l_{m_o}\sin\theta$ for the thickness and $\Delta c_p = c_p(\theta) - c_p(-\theta)$

$$\frac{\bar{v}}{W_\infty} = \frac{\alpha R_l}{6}\left(\frac{\delta_t}{c_o}\right)^2\left(\frac{1+2\epsilon}{\epsilon}\right)\frac{(1-\cos\theta)}{[\epsilon^2+\sin^2\theta]} \tag{27}$$

after simplifications.

The similarity between this result and the more exact answer (25) is significant. An example will help to show that a two dimensional approximation is adequate considering the approximations that have already been made. Figure 22 compares the variable portion of these two answers for the case that $\epsilon = 0.1$, i.e., a ten percent thick airfoil. The two dimensional assumption has already been used, and it will be used again in calculations that follow.

By comparing the magnitudes of the tip clearance velocities obtained from the perfect fluid model (Equation (6)) and equilibrium laminar flow model (Equation (26)), further confirmation of the relative importance of friction and inertia forces is possible. In the intermediate range of $\lambda^2 R_l \epsilon$, say $\lambda^2 R_l \epsilon = 50$ and for $\Delta c_p = 1.0$,

$$\frac{\bar{v}}{W_\infty} = \frac{W_t}{W_\infty} = \frac{\Delta c_p(\lambda^2 R_l \epsilon)}{24} = 2.08 \tag{28}$$

for equilibrium laminar flow if $\frac{f_a}{f_{m_o}} = 1.0$. For a perfect fluid

$$\frac{W_t}{W_\infty} = (\Delta C_p)^{\frac{1}{2}} = 1.00 \qquad (29)$$

The larger velocity in the case of equilibrium laminar flow is due to the fact that the frictional pressure drop is appreciably less than the one velocity head that occurs in the potential flow calculation. Therefore, a completely viscous solution of the tip clearance flow problem should be restricted to $\lambda^2 R_a \epsilon < 11$ as indicated in the previous section.

F. The Calculation of the Tip Clearance Velocity for a Stationary Blade with both Inertia and Friction Forces Included

In the range of clearances from $\lambda^2 R_a \epsilon = 11$ to $\lambda^2 R_a \epsilon = 125$ a more realistic model should include both the accelerations and the losses. This suggests using the Bernoulli equation with loss terms added. Therefore

$$P_1 + \tfrac{1}{2}\rho W_1^2 = P_2 + \tfrac{1}{2}\rho\left(W_t^2 + W_1^2\right) + \text{losses} \qquad (30)$$

P_1, P_2, and W_1 are the undisturbed values on the blade away from the clearance. The energy contribution from the flow along the blade ($\frac{\rho W_1^2}{2}$) is again assumed to be transported through the clearance unchanged, since the pressure gradient along the blade is small compared to the gradient across the blade.

The losses may take three forms: (1) an entrance loss which can be represented approximately by the form $\frac{k}{2}\rho\left(W_t^2 + W_1^2\right)$ where $0 \le k \le \frac{1}{4}$, the value of k depending on the sharpness of the entrance corner of the clearance [17], (2) a turbulent friction loss of the form

$C_f \frac{2\ell_o}{\delta_t} \frac{\rho}{2}\left(W_t^2 + W_1^2\right)$ where C_f could be approximated by $\frac{.078}{R_{\delta_t}^{1/4}}$, and (3) C_f becomes $\frac{12\nu}{\delta_t (W_1^2 + W_t^2)^{1/2}}$ if a laminar flow assumption is valid. The entrance loss is due to the separation and reattachment of the flow at the sharp corner as shown in Figure 17.

If C_f is assumed independent of W_t then W_t is given approximately by

$$\frac{W_t}{W_\infty} = \left\{ \frac{\Delta C_p - \left(k + \frac{2\ell_o}{\delta_t} C_f\right)\left(\frac{W_1^2}{W_\infty^2}\right)}{1 + k + \frac{2\ell_o}{\delta_t} C_f} \right\}^{\frac{1}{2}} \tag{31}$$

For laminar flow with this approximation

$$C_f \cong \frac{12\nu}{\delta_t \left[W_1^2 + W_\infty^2 \Delta C_p\right]^{\frac{1}{2}}} \tag{32}$$

and for turbulent flow

$$C_f \cong \frac{.078}{\left[\frac{\delta_t}{\nu}\left(W_1^2 + W_\infty^2 \Delta C_p\right)^{\frac{1}{2}}\right]^{\frac{1}{4}}} \tag{33}$$

In Reference 18 transition was reported to occur in slots in the range of Reynolds numbers from 2000 to 4000. Therefore a Reynolds number of 2500, based on the tip clearance and the tip clearance velocity, will be assumed to divide the flow regimes in the full length of the clearance.

G. The Effect of Blade Rotation on the Tip Clearance Flow

Thus far the analysis and experiments have been concerned with tip flows for a stationary blade near a stationary wall. This case is of little practical interest for in actual machines the stator blade tips are adjacent to the rotating hub and the rotor blade tips are moving relative

to the adjacent stationary wall. The tip clearance flow for the stationary blade and wall is, of course, much easier to study experimentally and it does isolate the influence of the pressure difference across the blade. At first it might be assumed that the effect of rotation simply could be added to the pressure flow, but a more careful investigation shows that this is not correct.

It is most convenient to view the clearance flow from a coordinate system attached to the blade so that the wall moves relative to the blade tip with the tip speed. For axial flow compressors and pumps the pressure surface leads the rotation so that the flow required by the "no-slip" condition at the moving wall is in the direction from the pressure to suction side, the same as for the flow resulting from the pressure differential.

A crude idea of the properties of the flow relative to the rotor blade tips can be obtained by considering mean velocity triangles for the flow in this region. Figure 19 shows two triangles, one in the free stream where U is the absolute velocity and W_∞ is the velocity relative to the blade, and a second triangle at a typical station in the case boundary layer. A blade is drawn in to show its position relative to the flow.

If the velocity, u, in the boundary layer can be described by a n^{th} root profile ($\frac{u}{U} = \left(\frac{y}{\delta}\right)^{\frac{1}{n}}$), then the flow incidence angle can be computed.

$$\alpha = \tan^{-1}\left\{\frac{1-\varphi_o\left(\frac{y}{\delta}\right)^{\frac{1}{n}}\tan\gamma}{\varphi_o\left(\frac{y}{\delta}\right)^{\frac{1}{n}}}\right\} - \beta_o^* \qquad (34)$$

if u_o is approximately constant through the layer. It is apparent from (34) and the diagram that the incidence angle increases through the layer

as the wall is approached. This has already been seen in the flow visualization experiments recorded in Figure 10. When this cross flow reaches the pressure side of a blade, the flow rolls up along the blade and forms a weak vortex. This vortex has been observed by others [8], and it was seen in the flow visualization experiments that will be described later in this section. This strong cross flow relative to the blade in the blade channels results in large curvature of the stream lines in the corner which is accompanied by strong pressure gradients along the blade near the tip.

A simplified mathematical model is used here to show the importance of the pressure variation along the blade due to the "scraping up" of the case boundary layer. Boundary layer flow in a corner can be computed approximately by assuming a uniform distribution of vorticity. The corner represents the intersection of the blade with zero tip clearance to the case wall moving relative to the blade. The boundary layer flow is assumed to intersect the blade and travel off at right angles. The boundary layer is represented by a region of twice the displacement thickness, δ^*, in which there is a uniform vorticity distribution, i.e., a linear velocity profile far from the corner. The value of the velocity at the wall is the component of the tip speed perpendicular to the blade. The idealized flow geometry is shown in Figure 20.

The equation governing the stream function ψ is $\nabla^2\psi = \frac{u_\infty \cos\beta_\infty^*}{2\delta^*}$ with the boundary conditions that $\psi = 0$ on the x and y axis and $\psi = \psi_1$ on the other flow boundary. The values of ψ far upstream and downstream are

$$\psi_{x=\infty} = u_0 \cos\beta_0^* \left\{ \frac{y^2}{4\delta^*} - y \right\} \tag{35}$$

$$\psi_{y=\infty} = u_0 \cos\beta_0^* \left\{ \frac{x^2}{4\delta^*} - x \right\} \tag{36}$$

For an approximate solution valid in the corner, the infinity conditions will be assumed to exist at $x = 2\delta^*$ and $y = 2\delta^*$. A solution

$$\psi = -u_0 \cos\beta_0^* \delta^* \left[\frac{y}{\delta^*} - \frac{1}{4}\left(\frac{y}{\delta^*}\right)^2 \right]\left[\frac{x}{\delta^*} - \frac{1}{4}\left(\frac{x}{\delta^*}\right)^2 \right] \tag{37}$$

is used even though it only satisfies the differential equation on the boundaries and the boundary conditions. The velocity along the y axis is

$$-\left.\frac{\partial\psi}{\partial x}\right|_{x=0} = u_0 \cos\beta_0^* \left[\frac{y}{\delta^*} - \frac{1}{4}\left(\frac{y}{\delta^*}\right)^2 \right] \tag{38}$$

The Bernoulli equation can be used to determine the pressure on the y axis if the Bernoulli constant is evaluated on the stream line that forms the corner. Thereby

$$\frac{P - P_1}{\frac{1}{2}\rho u_0^2 \cos^2\beta_0^*} = 1 - \left[\left(\frac{y}{\delta^*}\right) - \frac{1}{4}\left(\frac{y}{\delta^*}\right)^2 \right]^2 = I\left(\frac{y}{\delta^*}\right) \tag{39}$$

This pressure distribution is plotted on Figure 23. The pressure increase along the blade toward the tip is seen to be appreciable and must affect the tip clearance flows since the clearance space is small compared to the boundary layer thickness.

To investigate the effects of rotation on the pressure distribution at the blade tip experimentally, a two dimensional hydrofoil was mounted normal to a large disc that could rotate and hence simulate the relative

motion of the wall. The disc which had a radius of eight times the blade chord was driven by a variable speed motor. A static pressure tap was located on the pressure side of the blade 0.020 inches from the tip. The whole assembly was mounted in a slow speed free-surface flume. Thus the pressure measurements could be made easily for various ratios of free stream velocity to rotational speed and various stagger angles by changing the location of the foil on the disc. The increase in pressure, as shown in Figure 24, is of sufficient magnitude that it should be taken into account in a calculation of the tip clearance velocity. The primary conclusions from this experiment are that: (1) the pressure difference and the rotational shear flow cannot be treated separately since the rotational motion modifies the pressure field, and (2) the blade stagger angle is important in determining the pressure field near the blade tip.

Flow visualization experiments were conducted with the rotating disc equipment. Three noteworthy observations were made: (1) the tip clearance velocities were increased markedly as the rotational speed increased, (2) there appeared to be two regions of tip clearance flows, one close to the rotating wall in which the flow traveled with the disc, the other a generally larger region where the tip flow also felt the influence of the free stream flow, and (3) a "scraping" flow vortex was observed near the leading surface of the blade. The significance of these observations will be discussed in the next section.

H. The Calculation of the Tip Clearance Velocity with Rotational Effects Included

A calculation of the velocity in the tip clearance that proceeds from the model which has been developed cannot hope to be valid near the case where the velocity must be the tip speed relative to the blade. Fortunately the flow visualization observation indicates that only a small layer is completely dominated by the rotation of the machine. It will be assumed that in the remainder of the clearance the Bernoulli equation approach used in the previous sections is still valid after a correction for the increased kinetic energy normal to the blade has been made.

The Bernoulli equation in a rotating coordinate system is

$$P + \tfrac{1}{2}\rho W^2 = \text{const.} \tag{40}$$

if the radial motion of the stream lines is negligible and W is the velocity relative to the coordinate system. Applying (40) to the flow through the clearance space is possible if the loss of energy along the stream line is taken into account. Therefore

$$P_1 + \tfrac{1}{2}\rho\left(W_1'^2 + W_1''^2\right) = P_2 + \tfrac{1}{2}\rho\left(W_t^2 + W_t''^2\right) + \text{losses} \tag{41}$$

where W_t is the velocity in the clearance normal to the blade, W_1' is the component of the free stream velocity normal to the blade, and W_1'' is the component along the blade. W_1' and W_1'' can be computed using the mean velocity triangle of Figure 19. The values used for the tip clearance velocity calculations will be taken at $y = \delta_t/2$. It follows that

$$W_1' = W_1 \sin\alpha \tag{42}$$

$$W_1'' = W_1 \cos\alpha \tag{43}$$

$$W_1 = \frac{\varphi_o U_o}{\cos(\beta_o^* + \alpha)} \left(\frac{\delta_t}{2\delta}\right)^{\frac{1}{n}} \tag{44}$$

and α is given by (34). A consequence of this model of tip flows is that the boundary layer thickness, boundary layer profile shape, and the blade tip stagger angle become parameters in velocity calculation.

W_1' increases as the tip clearance is reduced so the relative total head near the wall is effectively increased. The primary effect of this increase in total head is to increase the tip clearance velocity over that for the stationary case. In using P_2 on the right hand side of (41), it is assumed that the pressure field on the suction side of the blade is not materially affected by the rotation or the presence of the tip clearance. The losses, as they have been enumerated before, are entrance loss $\frac{k}{2}\rho\left(W_t^2 + W_1''^2\right)$ and turbulent or laminar friction $\frac{\rho C_f}{2}\left(\frac{2l_o}{\delta_t}\right)\left(W_t^2 + W_1''^2\right)$ where $C_f = \frac{.070}{R_o \delta_t^{1/4}}$ for the turbulent case and $C_f = \frac{12\nu}{\delta_t\left[W_t^2 + W_1''^2\right]^{1/2}}$ for laminar flow. A Reynolds number of 2500 will be assumed to divide the flow from either completely turbulent or completely laminar for the full width of the clearance.

Again considering two dimensional sections normal to the blade, then

$$\frac{W_t}{W_\infty} = \left\{\frac{\Delta C_p + \left(\frac{W_1'}{W_\infty}\right)^2 - \left(k + \frac{2C_f l_o}{\delta_t}\right)\left(\frac{W_1''}{W_\infty}\right)^2}{1 + k + \frac{2C_f l_o}{\delta_t}}\right\}^{1/2} \tag{45}$$

if C_f is assumed independent of W_t. For laminar flow

$$C_f \cong \frac{12\nu}{\delta_t\left[W_1''^2 + W_\infty^2 \Delta C_p\right]^{1/2}} \tag{46}$$

while for turbulent flow

$$C_f \cong \frac{.078}{\left[\delta_t/2 \left(W_1''^2 + W_\infty^2 \Delta C_p\right)^{1/2}\right]^{1/4}} \qquad (47)$$

It is interesting to note from (45) by using a few numerical examples that: (1) if the pressure side edge of the blade is rounded, $\beta = 0$ then $\frac{W_t}{W_\infty}$ is generally less than ten percent high by neglecting the viscous losses for the range of clearances in general use in turbomachinery ($\lambda^2 R_t \epsilon > 125$), (2) if both the viscous forces and entrance loss are neglected when they should be included, an error of the order of twenty percent is made. It is again concluded that the inertia forces are more important than the viscous forces in determining the tip clearance velocity for the clearances of practical importance.

Since no direct method of checking the tip clearance velocity calculations is possible, estimates of the losses due to the clearance flow will be made using these calculations and the results compared with efficiency measurements. An unfortunate weakness is that more assumptions must be made before the loss calculations are possible.

I. Tip Clearance Flow Losses

A mathematical model has been constructed to compute the tip clearance flow as a function of the chord line coordinate. If in addition an assumption of a loss mechanism is made, the tip losses can be computed. The total loss of power will be assumed to be the flux of kinetic energy associated with the flow normal to the blade. Probably some additional loss is introduced by the friction in the tip clearance, but unless

the tip clearance is very small these losses are not large. It will be shown in a later section that the vortex sheet formed by the tip clearance flow entering the free stream flow rolls up into a vortex. The loss assumption implies that the flux of kinetic energy normal to the blade chord creates the rolled up vortex that is eventually dissipated without recovery.

The total loss of power for the N blades in a blade row is therefore

$$\frac{\rho W_\infty^3}{2} N c_0 \delta_t \int_0^1 \left(\frac{W_t}{W_\infty}\right)^3 d\left(\frac{x}{c_0}\right) \qquad (48)$$

where X is the coordinate along the blade chord.

The drop in efficiency due to the clearance flow loss can be computed when the work coefficient, $\bar{\psi}'$, has been determined. Actually $\bar{\psi}'$ depends upon the tip clearance. Three effects that modify $\bar{\psi}'$ are: (1) as the clearance increases the pressure loading at the tip drops off due to the acceleration of flow into the clearance, and the torque is reduced, (2) the effective area of the blading is reduced as the clearance increases which also reduces the torque, and (3) the increase in the pressure loading at the tip due to the rotation becomes less important as the tip clearance increases which again reduces the torque. These three effects can be taken into account approximately to compute the variation of $\bar{\psi}'$ with tip clearance.

$\bar{\psi}'$ is defined as

$$\frac{T}{\pi R_0^3 \left(\frac{\rho U_0^2}{2}\right)\left(1-K^2\right)\bar{\varphi}} \qquad (49)$$

where T is the torque required to drive the machine to produce a flow

rate $\bar{\varphi}$. The computation of a corrected $\bar{\psi}'$ reduces to a calculation of the torque requirement of the machine.

It was shown previously that the pressure distribution on the pressure side of the tip of a blade could be computed adequately from the potential flow into a slot for tip clearances of practical importance. With this model the total force reduction on the pressure side of the blade can be computed by using (7) by an integration along the blade.

$$\int_0^{C_0}\int_{\delta_t}^{\infty}(P-P_1)\,dx\,dy=\frac{\rho}{2}\int_0^{C_0}W_t^2\,dx\int_0^1 q_\beta^2\frac{dy}{dq_\beta}\,dq_\beta=-\frac{\delta_t}{40}\rho C_0 W_\infty^2 C_{L_0} \quad (50)$$

where q_β is the velocity on the y axis divided by W_t. $\frac{W_t}{W_\infty}\cong(C_{L_0})^{\frac{1}{2}}$ is certainly adequate for this computation since only a small correction term is being computed.

To take into account the pressure due to the "scraping" flow, the flow model introduced in Section III-G will be superimposed directly on the previously calculated flow into a slot. Integrating (39) the force increase along the blade is

$$\int_0^{C_0}\int_{\delta_t}^{2\delta^*}(P-P_1)\,dx\,dy=C_0\delta^*\frac{\rho U_0^2}{2}\cos^2\beta_0^*\left[\frac{14}{15}-\left(\frac{\delta_t}{\delta^*}\right)+\frac{1}{3}\left(\frac{\delta_t}{\delta^*}\right)^3-\frac{1}{8}\left(\frac{\delta_t}{\delta^*}\right)^4+\frac{1}{80}\left(\frac{\delta_t}{\delta^*}\right)^5\right] \quad (51)$$

which is

$$C_0\delta^*\frac{\rho U_0^2}{2}\cos^2\beta_0^*\left[\frac{14}{15}-G\left(\frac{\delta_t}{\delta^*}\right)\right] \quad (52)$$

if

$$G\left(\frac{\delta_t}{\delta^*}\right)=\left(\frac{\delta_t}{\delta^*}\right)-\frac{1}{3}\left(\frac{\delta_t}{\delta^*}\right)^3+\frac{1}{8}\left(\frac{\delta_t}{\delta^*}\right)^4-\frac{1}{80}\left(\frac{\delta_t}{\delta^*}\right)^5 \quad (53)$$

It follows that the net torque increase on N rotor blades at a tip stagger angle of β_o^* is

$$\frac{\rho}{2} N R_o c_o \cos\beta_o^* \left[\delta^* u_o^2 \cos^2\beta_o^* \left(\frac{14}{15} - G\left(\frac{\delta_t}{\delta^*}\right) \right) - \frac{\delta_t}{2\sigma} W_\infty^2 C_{L_o} \right] \quad (54)$$

by considering the total force reduction to be applied at the tip radius.

The total integral of torque is therefore

$$T = \frac{\rho u_o^2 N}{2} \left[\int_{R_i}^{R=\delta_t} \frac{\varphi^2 c c_L R dR}{\cos\beta^*} + R_o c_o \cos^3\beta_o^* \delta^* \left\{ \frac{14}{15} - G\left(\frac{\delta_t}{\delta^*}\right) \right\} - \frac{\delta_t}{2\sigma} \frac{R_o c_o \varphi_o^2 C_{L_o}}{\cos\beta_o^*} \right] \quad (55)$$

Thus $\bar{\Psi}'$ can be computed from (49) giving

$$\bar{\Psi}' = \frac{N}{\pi \bar{\varphi} (1-K^2)} \left[\int_K^{1-\delta_t/R_o} \frac{(c/R_o)\varphi^2 C_L (R/R_o) d(R/R_o)}{\cos\beta^*} + \left(\frac{c_o}{R_o}\right)\left(\frac{\delta^*}{R_o}\right) \cos^3\beta_o^* \right.$$
$$\left. \times \left\{ \frac{14}{15} - G\left(\frac{\delta_t}{\delta^*}\right) \right\} - \frac{(\delta_t/R_o)(c_o/R_o)\varphi_o^2 C_{L_o}}{2\sigma \cos\beta_o^*} \right] \quad (56)$$

For most computations of the efficiency drop where small changes of δ_t are made from a point where $\bar{\Psi}'$ is known, $\bar{\Psi}'$ can be considered a constant. Therefore ΔE, the efficiency drop, can be computed directly from

$$\Delta E = \frac{\left(\frac{c_o}{R_o}\right) N \left(\frac{\delta_t}{R_o}\right) \varphi_o^3 \int_0^1 \left(\frac{W_1}{W_\infty}\right)^3 d\left(\frac{x}{c_o}\right)}{\pi \cos^3\beta_o^* (1-K^2) \bar{\varphi} \bar{\Psi}'} \quad (57)$$

It has already been shown that the acceleration of the flow is much more important than the viscous pressure drop for the Reynolds numbers and tip clearances generally used in compressors, so the viscous terms will be neglected completely in the calculation of the clearance velocity. Equation (39), evaluated at $y = \frac{\delta_t}{2}$, is used to correct for the pressure increase on the blade due to the impact of the boundary layer flow. Therefore

$$\frac{W_1}{W_\infty} \cong \left[\Delta C_p + \frac{\cos^4\beta_\infty^*}{\varphi_\infty^2}\, I\left(\frac{\delta_t}{2\delta^*}\right)\right]^{\frac{1}{2}} \tag{58}$$

If the integral in (57) is replaced by its mean value, C_{L_∞} is evaluated as $\frac{S_\infty}{C_\infty}\,\frac{\psi'_\infty}{\varphi_\infty}\cos\beta_{\infty_\infty}$ and N as $2\pi\,\frac{R_\infty}{C_\infty}\left(\frac{C_\infty}{S_\infty}\right)$, then the efficiency drop for a rotor blade row is

$$\Delta E = \frac{2\left(\frac{\delta_t}{R_\infty}\right)\left(\frac{C_\infty}{S_\infty}\right)\varphi_\infty^3\left[\frac{S_\infty}{C_\infty}\,\frac{\psi'_\infty}{\varphi_\infty}\cos\beta_{\infty_\infty} + \frac{\cos^4\beta_\infty^*}{\varphi_\infty^2}\, I\left(\frac{\delta_t}{2\delta^*}\right)\right]^{\frac{3}{2}}}{\bar{\varphi}\,\bar{\psi}'\,(1-K^2)\cos^3\beta_\infty^*} \tag{59}$$

Usually $\varphi_\infty \approx \bar{\varphi}$, $\psi'_\infty \approx \bar{\psi}'$ and $\beta_{\infty_\infty} \approx \beta_\infty^*$, so using these approximations (59) reduces to

$$\Delta E = \frac{2\left(\frac{\delta_t}{R_\infty}\right)}{(1-K^2)\cos\beta_\infty^*}\left[\frac{S_\infty}{C_\infty}\,\frac{(\bar{\varphi}\bar{\psi}')}{\cos\beta_\infty^*}\right]^{\frac{1}{2}}\left[1 + \frac{C_\infty}{S_\infty}\,\frac{\cos^3\beta_\infty^*}{(\bar{\varphi}\bar{\psi}')}\, I\left(\frac{\delta_t}{2\delta^*}\right)\right]^{\frac{3}{2}} \tag{60}$$

Several authors have reported efficiency measurements on compressors as a function of tip clearance. The conclusion is the same from all of these sources, namely, the tip losses are a very important factor in pump and compressor performance. For example, Fickert [19] reports that the peak efficiency dropped three percent when the radial clearance was increased from 0.020 inches to 0.040 inches. Peter De Haller of Sulzer Brothers, Switzerland [20], reports an almost linear drop in peak efficiency of a commercial compressor from ninety-three percent at 0.020 inch clearance to eighty-four percent at 0.080 inch. Unfortunately, the complete blade design data is not available for these cases so a comparison with the theory is not possible. One source, Ruden [21], reports very detailed observations of a single stage fan's performance as a

function of radial clearance and also gives the details of the blade design. To supplement this data, the efficiency of the axial flow pump described in Part II was measured for three tip clearances. The clearances were chosen to cover the small clearances that Ruden did not consider. The measurements in the pump were made by detailed surveys before and after the rotor blade row with the pump operating at its design flow rate. The efficiency curves for these experiments and those of Ruden are plotted on Figure 25. The work coefficient curves are plotted on Figure 26.

The work coefficient curve is interesting in that it bears out the statement that the variation of $\bar{\psi}'$ with tip clearance is negligible, at least for the range of clearance of practical interest.

The use of the tabulated blade design for these two cases makes possible a direct comparison of the theory (Equation (59)) and the experiments. If the experimental efficiency curves are extrapolated to zero tip clearance, this intercept will be used as the efficiency at zero tip clearance for the theoretical efficiency curve. The resulting theoretical efficiency curves are plotted with the corresponding experiments on Figure 25.

The good agreement of the theory with the experiments, even for the smaller clearances, is probably due to the reasonably high Reynolds numbers for each experiment (Ruden [21] $R_{\ell} = 360,000$ and for the pump facility experiments $R_{\ell} = 280,000$). For even the smallest clearance tested ($\lambda = 0.046$), $\lambda^2 R_{\ell} \epsilon$ equaled 50.

The importance of the tip clearance flow losses can not be overlooked in view of the constant struggle for a two to three percent gain in efficiency

by compressor designers. It is hoped that a more thorough understanding of these flows should encourage attempts to build smaller clearances into new machines.

IV. FLOW OUTSIDE THE TIP CLEARANCE

A. Introduction

When the Kutta condition is applied along a slot in a wing, the stream line at the slot edge separates from the wing. The flow in the slot enters the main flow at some angle, so the separated stream line is also a discontinuity surface. Thus a pair of vortex sheets bound the flow from the slot while the main stream flow goes by on the outside in a different flow direction. Part IV will be devoted to a study of the motion of these vortex sheets as they travel downstream. Observations of cavitation were made to show that the sheets actually roll up along their leading edges to form vortices.

B. Observations of Tip Vortex Cavitation in Axial Flow Pumps

Observation of the tip vortex in liquids is made possible because of the phenomenon of cavitation. The rotating flow of a vortex causes a positive pressure gradient radially outward from the vortex center. Thus the pressure at the center of the vortex is reduced below the surrounding pressure field. If the surrounding pressure is sufficiently low, the pressure in the core of the vortex can drop below the vapor pressure of the liquid and the liquid will boil locally or cavitate. Four techniques can be used to obtain cavitation in a pump: (1) at a constant system pressure an increase in the rotative speed of the machine dynamically reduces the pressure near the blades, (2) the static pressure in the entire pump can be reduced, (3) a combination of the first two methods can be used, and (4) simulated cavitation can be obtained by injecting a gas into the center

of the vortex. In this case the vortex pressure field dominates the buoyant forces and the vortex core is traced out by a gas-filled cavity. In these experiments the rotative speed was increased and the variable system pressure feature of the circuit was used.

A complication inherent in cavitation work in a closed circuit at reduced pressures is the dissolved air content of the water. Most of this air must be removed or it will come out of solution during the experiments thereby obscuring and invalidating the results. In these experiments de-aeration was accomplished by running the machine under high vacuum for periods up to six hours. The air content was maintained at from six to ten parts per million during all of the cavitation experiments.

It was found that with blades with sharp corners on the pressure side edge, the flow separated and cavitation in the clearance space resulted. Rounding this edge eliminated this type of cavitation. The difference is shown in Figure 30 where the blade on the left has a sharp edge while the blade on the right has a radius of 0.020 inches on the edge. The minimum radius required to eliminate this cavitation was found to be approximately equal to the tip clearance over the range of clearances that were tested. All of the rotor blades were rounded on the pressure side to prevent this type of cavitation while a study of vortex cavitation was being conducted.

A logical first step in exploring cavitation in an axial flow pump and its relation to tip clearance flows was to determine visually the dependence of the inception point of cavitation on tip clearance. It should be recalled that it is only recently [11] that tip flows were suspected of

governing cavitation inception in pumps. Previously [22] blade surface cavitation had always been assumed to occur first.

For each run the tip clearance was adjusted and measured through the calibrated holes in the machine case. Then with the pump running at a rotative speed of 600 rpm and the desired flow rate, the system pressure was lowered until cavitation was regularly observed near a majority of the blades. This pressure was recorded and defined as being the "incipient" point. The rotor blades are generally critical for cavitation in most pumps because the blade row before the rotor is relatively lightly loaded and the blade rows that follow have the benefit of the static pressure rise through the rotor.

The cavitation inception pressure should scale from one rotative speed to another in a manner similar to a pressure coefficient, except that the pressure of importance is the difference between some representative ambient pressure and the vapor pressure of the liquid (P_v). Therefore the cavitation number $K = \frac{P_\infty - P_v}{\frac{1}{2}\rho W_\infty^2}$ is used to compare cavitation data. P_∞, as defined for these experiments, is the static pressure on the case immediately before the rotor blade row. W_∞ is the mean velocity relative to the rotor blade tip. Appendix B gives the details of the calculations required to arrive at K. A higher value of K means that cavitation started at a higher value of system pressure or a lower rpm than for a smaller K. Essentially, the larger the cavitation number the worse is the cavitation performance of the machine.

The incipient cavitation number is plotted as a function of tip clearance for four flow rates on Figure 27. The upturn of the curves for

the small tip clearances was a surprising result which will be discussed in some detail.

In conjunction with the visual observations of cavitation, a series of photographs was taken of tip vortex cavitation for the purpose of recording the change of the vortex structure with tip clearance. A four by five inch view camera was used with lighting supplied by two Edgerton type single flash lamps triggered by a commutator on the shaft. The photographs were taken at cavitation numbers below inception to avoid the difficulty of photographing the sporadic cavitation near the incipient point. Figure 29 shows a compilation of these photographs comparing the cavitation for a number of tip clearances under identical operating conditions.

The vortex structure is predominant for all of the clearances except for the very smallest ($\lambda = 0.026$). It can only be conjectured why there was no vortex for $\lambda = 0.026$, but it is certainly true that viscous forces must dominate the flow for this tip clearance. This clearance is much smaller than is in use in general turbomachine practice.

The photographs will be discussed in more detail after another experiment is described. It has been pointed out in Section III-C that one of the primary features of the tip clearance flow is the relative motion between the blade and the end wall. Therefore it was of interest to investigate whether or not presence of this motion would cause any significant difference in the vortex cavitation. It has been already shown that the tip clearance velocity is increased appreciably by the rotational motion. A measure of the importance of the rotation can be gained by a comparison of the incipient cavitation data from the pump to data taken on a single

stationary hydrofoil with tip clearance to a wall. The two dimensional hydrofoil used was approximately of the same geometry as the tip of the pump's rotor blade. The incipient cavitation number was measured for a selected number of angles of attack and tip clearances with the test section wall of the High Speed Water Tunnel in the Hydrodynamics Laboratory. Appendix B describes the method used to compute the angle of attack settings so they were equivalent to given flow rates of the pump. The results of this experiment are shown on Figure 28. This figure can be compared directly with Figure 27 to show the striking difference between the cavitation inception for the stationary and rotating cases. Photographs of the cavitation were also taken for each configuration, samples of which are shown in Figure 31.

C. Discussion of the Cavitation Experiments

The cavitation for large tip clearances for the stationary and rotating cases (Figure 29 D and Figure 31 C) appear similar, but the structure and location of the cavitating core diverge widely for the smaller clearances (Figure 29 B and Figure 31 B). Significantly the vortex does not appear near the leading edge of the stationary blade as it does in the machine. In fact, the location of the vortex for the stationary case is behind the quarter chord point for all tip clearances.

A stationary hydrofoil in a wall boundary layer must lose circulation proportional to the velocity profile; hence the circulation shed at the tip increases with tip clearance. The underpressure of a vortex is proportional to its strength and concentration, so cavitation will start

at higher K's when the tip is out of the region of important viscous effects, but what causes the opposite variation in the rotating case?

The minimum pressure region on an airfoil of ordinary design is near the leading edge of the suction side for any positive angle of attack. Near zero angle of attack the minimum pressure region moves back to near the midchord on the suction surface of the blade. If the angle of attack is reduced still more, the minimum pressure appears on the pressure side of the blade. Thus even though the underpressure of the vortex may remain roughly constant with tip clearance changes in the rotating case, the vortex in the pump (see Figure 29) moves into a region where the blade underpressure is sufficiently low to make the cavitation start at higher values of K. Consequently the change in the location of the vortex explains the marked upturning of the cavitation inception curves from the pump. This viewpoint is confirmed by the variation of the magnitude of the peaks in the cavitation number for the small clearances. At the reduced flow rates where the peak underpressures are the largest, there are correspondingly higher peaks in the cavitation numbers (see Figure 27). The peaks in the cavitation number curves for positive angles of attack can thus be explained, but a different behavior would be expected near the zero angle of attack. The $\bar{\varphi} = 0.48$ curve in Figure 27 shows the upturning of the K curve when the vortex starts to form in the low pressure region near mid-chord. In general, the conclusion can be made that the blade surface pressure distribution governs the inception of cavitation as affected by the flow rate. This is also the case for ordinary blade surface cavitation.

The reasons for the difference in the location of the vortex between the stationary and rotating case is the strength and direction of the tip clearance flows. The stronger clearance flow for the rotating case results in a larger angle between the vortex and the blade chord line, and therefore the vortex starts forward of the point where it would on the stationary blade. As the tip clearance increases, for both cases the flow through the clearance redirects itself to conform more with the free stream flow direction. This greatly affects the rotating blade, for the vortex has a long way to travel to reach its free stream location near the trailing edge. The vortex on the stationary blade, in contrast, requires comparatively little relocation to reach its final position at the rear of the blade.

The conclusions of the cavitation experiments are:

(1) A vortex is formed by the interaction of tip clearance flow with the flow past the blade. The vortex location and structure are strongly affected by the flow due to machine rotation as is seen by comparison of the vortex formed on a stationary hydrofoil and on a blade in the pump.

(2) For the optimum cavitation performance of a pump, the tip clearances should not be the smallest that it is possible to construct.

D. Observations on the Formation of a Vortex Due to a Thin Jet Entering a Stream

It has been confirmed by the cavitation experiments that the tip

clearance flows create a vortex sheet that deforms into a vortex. To make an analysis of the vortex, the most simple model possible that retains its essential physical character is desired. To study the flow in the hope of eliminating the unimportant quantities, a simulated tip clearance was set up in a low speed flume with windows in the walls. A flat plate was installed perpendicularly to the side wall of the tunnel. A small notch machined in the plate formed a tip clearance slot in the corner. The slot was supplied with a steady flow of water from above to complete the model. Dyed water and oil droplet injections were used to study the flow. The result for all ratios of jet velocity to free stream velocity was a vortex formed along the intersection of the two flows. A schematic diagram of the flow is shown in Figure 32. Further experiments showed that removing the corner had no effect on the rolling up process. The boundary layer on the wall was also shown to be unimportant, thereby simplifying the model even more. The conclusion is that a thin jet intersecting a through flow at an angle other than zero rolls up and forms a vortex. The result undoubtedly also applies to jets of more general shape [23], but it would be more difficult to observe the vortex experimentally.

E. The Formation of the Vortex Sheet Due to a Jet Entering a Stream and Its Roll Up Into a Vortex

The boundary region between the jet and the through flow velocity may be represented by a vortex sheet of two components. One component in the jet direction is due to the displacement of the through flow over the jet requiring a transition from zero to the free stream velocity. The

second component is due to the velocity gradient in the direction of the jet flow, and so it is perpendicular to the jet. Figure 33 shows by cavitation physical evidence of the existence of this vortex sheet.

For a first consideration of the rolling up of the vortex sheet analytically, a linearized computation of the deformation of the discontinuity surface formed by a thin rectangular jet entering a through flow at right angles along a wall will be performed. The linearization is made possible by assuming the entering jet velocity is large compared to that of the through flow. The immediate consequence of this supposition is that the jet is turned very little by the through flow and the geometry of the discontinuity surface can be considered in two dimensional sections through the jet perpendicular to its original direction. In these planes only the vorticity due to through flow going around the jet is significant.

As the flow leaves the tip clearance, the vorticity is created and thence forward it is transported by the jet velocity away from the clearance and moves about by its self-induced velocity. Therefore if the original distribution is established, vortex laws can be used to calculate step by step the motion of the vortex sheet. The time base is the distance traveled away from the slit divided by the velocity of the jet.

The geometry at the initial instant was idealized as shown in Figure 34. For the initial instant the jet was considered rigid and the strength of the vortex sheet computed using the velocities on the boundaries. The circulation distribution must be lumped in a finite group of vortices to make the computations feasible. The grouping also eliminates the difficulty of the velocity singularity at the external corner (A). For

the computational purposes the initial geometry as shown in Figure 34 was replaced with twenty-two vortices of equal strength. The vortices were located to represent the sheet strength distribution along the initial shape. The vortex filaments were considered to be infinite in extent which introduced an error especially near the initial instant. The remainder of the vortex sheet was assumed to remain undeformed and to extend to infinity in the negative X direction. The method of images was used to give the boundary condition of no velocity component normal to the wall.

The formulas for calculating the change in the location of the i^{th} vortex are

$$\frac{\Delta X_i}{\delta_t} = \frac{\Delta t^*}{\pi^2}\left[\sum_{k} \frac{d_{ik}}{\lambda_{ik}^2} - \sum_{k'} \frac{d_{ik'}}{\lambda_{ik'}^2}\right] + \frac{\Delta t^*}{2\pi}(\theta_2 - \theta_1) - \Delta t^* \qquad (61)$$

$$\frac{\Delta y_i}{\delta_t} = \frac{\Delta t^*}{\pi^2}\left[\sum_{k'} \frac{h_{ik'}}{\lambda_{ik'}^2} - \sum_{k} \frac{h_{ik}}{\lambda_{ik}^2}\right] + \frac{\Delta t^*}{2\pi} \ln \frac{\lambda_2}{\lambda_1} \qquad (62)$$

where $\Delta t^* = \frac{\Delta Z}{\delta_t} \frac{U}{V}$. ΔZ is the change in the distance traveled in the jet direction, and $\frac{U}{V}$ is the ratio of through flow velocity to the jet velocity (see Figure 35 for other notation definitions). The second term on the right of each expression is the contribution of the remainder of the sheet. The geometry at each station only depends on the total of the Δt^*'s to that station, so this computation is good for all cases where the approximation applies.

Figure 36 shows the results of six steps of the computation. The rolling back characteristic of the motion is quite apparent showing that the model adequately represents the flow. The concentration of the vorticity

in the rolled back region is the vortex that has been shown experimentally, and its approximate strength could be evaluated by summing up the vortices in this area. Since the size of the vortex will also be of interest in later calculations, it is important to note that the size of the core is roughly determined by the amount of fluid entering the vortex from the jet. Actually, the tip clearance velocities are found to be of the same order as the free stream velocity. Therefore the assumption of a "stiff" jet is not applicable to the tip clearance problem, but the calculation has given some useful qualitative ideas for further calculation.

F. Formation of the Vortex Sheet Near a Blade Tip with Its Subsequent Rolling Up

A simplified airfoil model that will include both the rolling up and deflection features of the vortex formation can be developed to obtain the properties of the vortex. The two simplifications to be utilized are (1) nonviscous flow will be assumed, and (2) the blade will have a constant pressure difference along the chord. The blade can be represented by a flow with a velocity $W_\infty + u$ on the suction side of the chordline and $W_\infty - u$ velocity on the pressure side. W_∞ is the velocity from infinity and u is a constant perturbation velocity. By using Bernoulli's equation

$$\frac{P_1 - P_2}{\frac{1}{2}\rho W_\infty^2} = C_{L_\alpha} = \frac{4u}{W_\infty} \qquad \text{or} \qquad u = \frac{C_{L_\alpha}}{4} W_\infty \tag{63}$$

If this airfoil is normal to a wall with small clearance, the tip clearance velocity normal to the blade can be computed by Equation (6)

giving $\frac{W_t^2}{W_\infty^2} = C_{L_o} = 4\frac{u}{W_\infty}$, so the resultant tip velocity is

$$\left[(W_\infty - u)^2 + W_t^2\right]^{\frac{1}{2}} = W_\infty + u \tag{64}$$

if the kinetic energy along the blade is transported through the clearance without change. The angle of tip flow from the clearance (see Figure 37) is

$$\beta = \tan^{-1} \frac{4C_{L_o}^{\frac{1}{2}}}{4 - C_{L_o}} \tag{65}$$

Therefore a vortex sheet is created with equal velocities on each side, but a change in flow direction through the discontinuity surface is required. The sheet strength γ may be computed by considering Figure 37.

$$\frac{\gamma}{W_\infty} = \frac{2(W_\infty + u)}{W_\infty} \sin\frac{\beta}{2} = \frac{(C_{L_o})^{\frac{1}{2}}}{2}(4 + C_{L_o})^{\frac{1}{2}} \tag{66}$$

The transport velocity of the sheet V follows from the same consideration

$$\frac{V}{W_\infty} = \frac{(W_\infty + u)}{W_\infty} \cos\frac{\beta}{2} = \frac{1}{2}\left[4 + C_{L_o}\right]^{\frac{1}{2}} \tag{67}$$

Incidentally the angle of V with the chord line, $\frac{\beta}{2}$, must be the angle that the vortex lines make with the chord line, i.e., the vortex filaments are transported with the local velocity. Hence

$$\tan\frac{\beta}{2} = \frac{(C_{L_o})^{\frac{1}{2}}}{2} = \frac{2u}{W_t} \tag{68}$$

It is interesting to check the total magnitude of the circulation leaving the blade. At the trailing edge

$$\gamma c_o \sin\frac{\beta}{2} = \frac{W_\infty c_o C_{L_o}}{2} \tag{69}$$

which is the total lift circulation on the blade. Hence this calculation gives the local details of the shedding of the circulation from an airfoil with a small clearance to a wall.

The formation of the discontinuity surface has been computed, but a detailed study of the flow will show that this sheet of vorticity rolls back along its leading edge. The sheet must indeed deform, for the fluid coming from the clearance must collect along the leading edge of the sheet and hence modify the local surface geometry. A computation similar to the "stiff jet" calculation can be set up for considering the motion of the discontinuity surface if sections perpendicular to the undisturbed vortex sheet are considered (see Figure 38). The equations for the displacement of the i^{th} vortex are

$$\frac{\Delta x_i}{\delta t} = \frac{\Delta t^*}{4\pi}\left[\sum_{i'} \frac{d_{i i'}}{r_{i i'}^2} - \sum_{i} \frac{d_{i i}}{r_{i i}^2}\right] - \frac{\Delta t^*}{2\pi}(\theta_2 - \theta_1) + \frac{\Delta t^*}{2} \qquad (70)$$

and

$$\frac{\Delta y_i}{\delta t} = \frac{\Delta t^*}{4\pi}\left[\sum_{i'} \frac{h_{i i'}}{r_{i i'}^2} - \sum_{i} \frac{h_{i i}}{r_{i i}^2}\right] + \frac{\Delta t^*}{2\pi} \ln \frac{r_2}{r_1} \qquad (71)$$

if the sheet length is long compared to the tip clearance, and increments of length $\frac{\delta t}{2}$ of the vortex sheet are lumped in each vortex. t^* is $\left(\frac{\xi}{c_0}\right)\left(\frac{c_0}{\delta t}\right)(C_{L_0})^{\frac{1}{2}} = \frac{\left(\frac{\xi}{c_0}\right)(C_{L_0})^{\frac{1}{2}}}{\lambda \epsilon}$ for this case, where ξ is the coordinate along the vortex sheet in the direction of the vortex lines. The use of t^* again reduces all of the rolling up problems to one case. The patterns for six cases, up to $t^* = 10$ were computed to give some insight for making approximate rolling up calculations that extend over a wider range of t^*. These patterns are shown on Figure 39. Three features of these

patterns will be used to extend the rolling up calculations. They are: (1) the patterns form roughly closed circles, (2) the circles remain nearly tangent with the original sheet, and (3) there is little stretching of the sheet as it rolls up.

With these idealizations and some other assumptions, the strength and size of the vortex can be estimated as a function of t^*. The length of the vortex sheet that has been rolled up and the radius of the rolled up circle must be a function of t^* only, therefore

$$\frac{b}{\delta_t} = f(t^*) \tag{72}$$

and

$$\frac{r_c}{\delta_t} = g(t^*) \tag{73}$$

are defined. Assuming the sheet is unstretched during the rolling up permits the calculation of the circulation in the vortex, if $f(t^*)$ were known.

$$\Gamma^* = \frac{2\Gamma}{W_\infty c_o C_{L_o}} = \frac{2\gamma b}{W_\infty c_o C_{L_o}} = \lambda \epsilon \left(\frac{4 + C_{L_2}}{C_{L_o}}\right)^{\frac{1}{2}} f(t^*) \tag{74}$$

To compute $f(t^*)$ the rolling up process will be idealized as a cylinder rolling on a plane with the distance it rolls increasing the perimeter of the cylinder as it rolls. The velocity at the center of the core will be used for the rolling velocity. There are three contributors to this velocity: (1) the free stream velocity $(W_\infty + u)\sin\frac{\beta}{2}$, (2) the velocity due to the image core, and (3) the induced velocity of two semi-infinite vortex sheets. Actually the velocity at the center of the vortex in the X direction (see Figure 38) due to the two vortex sheets is zero, so a differ-

ential equation for Γ or $f(t^*)$ may be written in terms of the unknown function $g(t^*)$.

$$\frac{d\Gamma}{d\xi} = \frac{\gamma}{V}\left\{(W_\infty + u)\sin\frac{\beta}{2} - \frac{\Gamma}{4\pi(h_c + \delta_t)}\right\} \tag{75}$$

or

$$\frac{df}{dt^*} = \frac{1}{2} - \frac{f}{4\pi(1+g)} \tag{76}$$

The growth of the core depends on the y component of the velocity at the maximum elevation point, A, on the vortex. There is no contribution to the upward velocity at A from the two vortex cores because of the almost circular symmetry. Therefore the only contribution is due to the two vortex sheets. Using this fact, $g(t^*)$ can be computed as follows:

$$2\frac{dh_c}{d\xi} = \frac{1}{2\pi}\frac{\gamma}{V}\ln\frac{4h_c + 2\delta_t}{2h_c} \tag{77}$$

or

$$\frac{dg}{dt^*} = \frac{1}{4\pi}\ln\left(2 + \frac{1}{g}\right) \tag{78}$$

A numerical integration of this differential equation (78), gave approximately

$$g(t^*) = .14\,t^{*0.86} \tag{79}$$

If this result is substituted in (76), an approximate relation for $f(t^*)$ can be obtained by numerical integration.

$$f(t^*) = 1.00\,t^{*0.72} \tag{80}$$

In summary

$$\Gamma^* = \lambda\epsilon \left(\frac{4 + c_{L_o}}{c_{L_o}}\right)^{\frac{1}{2}} t^{*\,0.72} \tag{81}$$

and

$$\frac{r_c}{\delta t} = .14\, t^{*\,0.85} \tag{82}$$

where $t^* = \dfrac{(\frac{s}{c_o})(c_{L_o})^{\frac{1}{2}}}{\lambda\epsilon}$. These results were compared with the point vortex calculations, and the check was sufficiently good to warrant the use of these approximate formulas in further calculations.

G. The Estimation of the Inception of Cavitation

The incipient cavitation results from the axial flow pump facility give an opportunity to compare the results of the previous section with experiment. If the vortex is considered two dimensional at each station along its length, then the pressure field can be computed. A review of the properties of a rectilinear vortex will aid in obtaining the desired result. Consider a vortex of strength Γ and core size a (see Figure 40) then it is assumed for

$$\begin{aligned} r \le a \quad & q = \omega r \quad & \frac{1}{\rho}\frac{\partial P}{\partial r} = \omega^2 r \\ r \ge a \quad & q = \frac{\omega a^2}{r} \quad & \frac{P}{\rho} + \frac{1}{2}\left(\frac{\omega a^2}{r}\right)^2 = \frac{P_\infty}{\rho} \end{aligned} \tag{83}$$

Now

$$\Gamma = \int_0^{2\pi} (\omega a)\, a\, d\theta = 2\pi\omega a^2 \tag{84}$$

so

$$\omega = \frac{\Gamma}{2\pi a^2} \tag{85}$$

The vortex core will be associated with all of the fluid that has entered the region from the tip clearance, so $a \approx \Lambda_c + \delta_t$. Cavitation will be assumed to occur if the center of the core is at the vapor pressure so the pressure at $\Lambda = 0$ is equal to P_v , the vapor pressure. Therefore

$$\frac{P_v}{\rho} + \frac{\Gamma^2}{4\pi^2 a^2} = \frac{P_2}{\rho} \tag{86}$$

or

$$\frac{P_2 - P_v}{\frac{1}{2}\rho W_\infty^2} = \frac{\Gamma^2}{2\pi^2 a^2 W_\infty^2} \tag{87}$$

The cavitation number may be formed if the surrounding pressure field is given by $C_p = \frac{P_2 - P_\infty}{\frac{1}{2}\rho W_\infty^2}$. Expanding the cavitation number as

$$K = \frac{P_\infty - P_v}{\frac{1}{2}\rho W_\infty^2} = \frac{P_\infty - P_2}{\frac{1}{2}\rho W_\infty^2} + \frac{P_2 - P_v}{\frac{1}{2}\rho W_\infty^2} \tag{88}$$

gives

$$K = -C_p + \frac{\Gamma^2}{2\pi^2 a^2 W_\infty^2} \tag{89}$$

Making use of (81) and (82)

$$K = -C_p + \frac{C_{L_\alpha}(4 + C_{L_0}) f^2(t^*)}{8\pi^2 (1+q)^2} \tag{90}$$

There are two difficulties in applying this formula to any particular case. First, the vortex calculations were made with the blade represented by a pressure difference distributed along the chord line. Actually the blade has thickness so that a vortex line will not necessarily leave from the leading edge of the blade. A good estimate of the origin of the ξ

coordinate system can be made by locating the point on the suction surface of the blade with a slope equal to $\tan \frac{\beta}{2} = \frac{(C_{L_0})^{\frac{1}{2}}}{2}$. It has already been pointed out in the discussion of pump cavitation that the chordwise location of the vortex has a predominant influence on the inception of cavitation in pumps. The second difficulty in applying Equation (90) is that the lift coefficient C_{L_0} is not known. It was shown in Section III-G that the impact of the case boundary layer on the blade tip increased the blade loading at the tip. Some calculations were made of the pressure increase along the blade near the tip (see Equation (39) and Figure 23), and they can be used to compute a corrected lift coefficient

$$C_{L_0} = \frac{S_0}{C_0} \frac{\psi_0'}{\varphi_0} \cos \beta_{\infty_0} + \frac{\cos^4 \beta_0^*}{\varphi_0^2} I\left(\frac{\delta_t}{\delta^*}\right) \qquad (91)$$

where $\frac{S_0}{C_0} \frac{\psi_0'}{\varphi_0} \cos \beta_{\infty_0}$ is the free stream lift coefficient. The influence of this increase in lift is important as can be seen by the variation of the angle that the vortex makes with the chord line (see Figure 29) when it is remembered that the tangent of the vortex angle varies as the square root of the lift coefficient. The vortex angle decreases from approximately 20° for $\lambda = 0.046$ to about 10° for $\lambda = 0.32$.

It is important to note that the vorticity that has been included in the rolled up vortex comes only from the interaction of pressure difference leakage flow with the main stream. The vorticity associated with the shear profile due to the rotation is not included because it is fairly uniformly distributed over the whole region near the wall whether or not the vortex exists. It has been assumed that the only effect of machine rotation is to effectively increase the lift coefficient at the blade tip.

Using these two corrections an example is worked out here that can be compared with the data from the machine. Take for example λ = 0.16 and φ_o = 0.45 (ϵ = 0.08 and β_o^* = 57.4° for this blade set). $\frac{s}{c_o}\frac{w'}{\varphi_o}\cos\beta_{\infty_o}$ is 0.58 at the blade tip and $\frac{\delta_1}{\delta}$ is 0.53. The corrected C_{L_o} is 0.86 and the origin of the ξ coordinate system is $\frac{x^*}{c_o}$ = 0.16. Now

$$t^* = \left(\frac{\xi}{c_o}\right)\frac{(C_{L_o})^{\frac{1}{2}}}{\lambda\epsilon} = \left(\frac{x}{c_o} - \frac{x^*}{c_o}\right)\frac{(C_{L_o})^{\frac{1}{2}}}{\lambda\epsilon}\frac{1}{\cos\beta/2} \qquad (92)$$

therefore

$$t^* = 80\left(\frac{x}{c} - 0.16\right) \qquad (93)$$

A summary of the results of the calculations are tabulated below

x/c_o	$-C_p$	$\frac{\int^2 C_{L_o}(4+C_{L_o})}{8\pi^2(1+\varphi)^2}$	K
0.00	-0.10	0.00	-0.10
0.05	0.66	0.00	0.66
0.10	0.62	0.00	0.62
0.15	0.60	0.00	0.60
0.20	0.60	0.14	0.74
0.25	0.60	0.30	0.90
0.30	0.58	0.40	0.98
0.35	0.56	0.48	1.04
0.40	0.53	0.52	1.05
0.45	0.48	0.54	1.02
0.50	0.44	0.56	1.00
0.55	0.39	0.58	0.97
0.60	0.34	0.58	0.92

The peak value of the cavitation number, K = 1.05, is theoretically the incipient cavitation point of the machine. The measured value (Figure 27) in the machine at this tip clearance flow rate is K = 0.88 which is not a very satisfactory agreement. One cause of the discrepancy

is believed to be the existence of tension in the water, i.e., the core of the vortex can be reduced below the vapor pressure before the cavitation starts. This would considerably reduce the contribution of the vortex; for example if the full core were below the vapor pressure when the cavitation started, the contribution of the vortex in Equation (90) would be reduced by half. Evidence that negative pressures do exist was seen in the cavitation experiments. A hysteresis of approximately five to ten percent was measured between the starting and stopping values of K for vortex cavitation.

This calculation points out two important features of vortex cavitation: (1) the contribution to the cavitation number due to the vortex is appreciable with an improvement of more than fifteen percent over the maximum possible if the vortex could be eliminated, and (2) the resulting total cavitation number depends a great deal on the point where the vortex starts. For this case, if the vortex started at the leading edge instead of the sixteen percent chord position, the cavitation number would increase another ten percent. Thus, as it has already been pointed out, the location of the vortex is very important in determining the inception of cavitation in a pump.

REFERENCES

1. Sorensen, H. A., "Gas Turbines", Ronald Press, (1951), p. 97.

2. Wu, Chung-Hua, "Survey of Available Information on Internal Flow Losses Through Axial Turbomachines", NACA RM E50J13, (1951).

3. Carter, A. D. S., "Three-dimensional-flow Theories for Axial Compressors and Turbines", War Emergency Issue No. 41, pub. by Inst. Mech. Eng., (Reprinted in U. S. by ASME (1949) pp. 255-268).

4. Eichenberger, H. P., "Shear Flow in Bends", Office of Naval Research Contract N5ori07848, Technical Report No. 2, (1951).

5. Loos, H. G., "Analysis of Secondary Flow in the Stator of an Axial Turbomachine", Guggenheim Jet Propulsion Center Report on Air Force Contract 18(600)-178, Calif. Inst. of Technology, (1953).

6. Daugherty, R. L., "Hydraulics", McGraw-Hill Co., (1937), p. 209.

7. Fuller, T. W. and Acosta, A. J., "Report on Design and Construction of the Axial Flow Pump Test Facility", Hydrodynamics Laboratory Report E-12.13, Calif. Inst. of Technology, (1953).

8. Hansen, A. G., Herzig, H. Z., and Costello, G. R., "A Visualization Study of Secondary Flows in Cascades", NACA TN 2947, (1953).

9. Squire, H. B. and Winter, K. G., "The Secondary Flow in a Cascade of Airfoils in a Nonuniform Stream", Journal of the Aeronautical Sciences, Vol. 18, No. 4, (April 1951).

10. Bowen, J. T., Sabersky, R. H., and Rannie, W. D., "Theoretical and Experimental Investigations of Axial Flow Compressors", Mechanical Engineering Laboratory Report Part I, Calif. Inst. of Technology, (1949).

11. Guinard, P., Fuller, T., and Acosta, A. J., "An Experimental Study of Axial Flow Pump Cavitation", Hydrodynamics Laboratory Report E-19.3, Calif. Inst. of Technology, (1953).

12. Betz, A., "Uber die Vorgange an den Schaufel-enden von Kaplan-Turbinen", Hydraulische Probleme VDI-Verlag, (1926).

13. Bollay, William, "A Nonlinear Wing Theory and its Application to Rectangular Wings of Small Aspect Ratio", Zeitschrift fur Angewandte Mathematik und Mechanik Bd. 19 Nr. 1, (February 1939).

14. Milne-Thompson, L. M., "Theoretical Hydrodynamics", MacMillan, 2nd Edition, (1950).

15. von Karman, T. and Tsien, H. S., "Lifting-line Theory for a Wing in Nonuniform Flow", Quarterly of Applied Mathematics Vol. III, (April 1945).

16. Bateman, H., "Partial Differential Equations of Mathematical Physics", Dover, (1944), p. 243.

17. Daugherty, R. L., "Hydraulics", McGraw-Hill, (1937), pp. 218-221.

18. Shire, G. L., "The Viscous Flow of Air in a Narrow Slot", Aeronautical Research Council Current Paper No. 13, (1950).

19. Fickert, "The Influence of the Radial Clearance of the Rotor on the Compressor Efficiency", Part C of "The Influence of Physical Dimensions and Flow Conditions on Compressor Characteristics", Bureau of Ships 338, (1946), pp. 95-108.

20. DeHaller, P., Unpublished Data from Sulzer Brothers, Switzerland, (1953).

21. Ruden, P., "Investigations of Single-Stage Axial Fans", NACA TM 1062, (1937).

22. Stepanoff, A. J., "Centrifugal and Axial-flow Pumps", Wiley and Sons, (1948), Chapter 12, pp. 241-270.

23. Lu, Hish-Chia, "On the Surface of Discontinuity between Two Flows Perpendicular to Each Other", The Engr. Reports of National Tsing Hua University, Vol. IV No. 1, (1948).

24. Keenan and Keyes, "Thermodynamic Properties of Steam", Wiley and Sons, (1936).

APPENDIX A

NOTATION

a	Vortex core radius
b	Length of vortex sheet in vortex
c	Blade Chord
c_p	Pressure coefficient $\frac{P - P_\infty}{\frac{1}{2}\rho W_\infty^2}$
c_f	Friction coefficient = $\frac{\text{Shearing stress at wall}}{\text{Local dynamic pressure}}$
c_L	Lift coefficient = $\frac{\text{Lift force per unit length}}{\frac{1}{2}\rho W_\infty^2 c}$
d	Vertical distance in vortex sheet calculations
f	Vortex strength function
g	Vortex radius function
h	Horizontal distance in vortex sheet calculations
i	$\sqrt{-1}$
i, k	Summation indices
k	Loss coefficient for entrance loss
l	Blade thickness
l_m	Maximum blade thickness
n	Boundary layer profile exponent
p	Static pressure
P_v	Vapor pressure of a liquid
r	Radius
r_c	Vortex sheet radius
s	Blade spacing

t	Time
t^*	A dimensionless time
q, u, v, w	Velocities
W_t	Tip clearance velocity normal to the blade
W_∞	Velocity relative to the blade
$\bar{u}, \bar{v}$	Mean velocities
u_o	Tip rotative speed of a machine
x, y, z	Coordinates
A	A point of interest
D	Machine outside diameter
E	Efficiency
G	Pressure loading function
I	Pressure distribution function
K	Cavitation number $\frac{P_\infty - P_v}{\frac{1}{2} \rho W_\infty^2}$
N	Number of blades
P	Power
R	Radius in machine
R_i	Hub radius in machine
R_o	Tip radius in machine
R_e	Reynolds number $\frac{W_\infty C_o}{\nu}$
T	Torque
U, V	Velocities
α	Angle of attack or flow incidence angle
β	Angle

β^* Stagger angle of rotor row (angle between chord line and machine axis)

β_∞ Mean flow angle

δ Angle

δ_2 Exit angle from entrance vanes of a machine

γ Vortex sheet strength - Circulation per unit length

δ Boundary layer thickness

δ^* Displacement thickness of boundary layer

δ_t Tip clearance

κ Hub Ratio R_i/R_o

σ Contraction ratio of a jet

λ Dimensionless tip clearance δ_t/l_{m_o}

ω Rotational frequency

Δ Change in any quantity

ϵ Thickness ratio of the blade tip l_{m_o}/c_o

Γ Circulation

Γ^* Dimensionless circulation $\dfrac{2\Gamma}{W_\infty C_L C}$

ξ Coordinate along vortex sheet

θ Angular coordinate

τ A complex plane $re^{i\theta}$

χ A complex plane $x + iy$

μ Viscosity

ρ Density

ν Kinematic viscosity μ/ρ

φ Complex velocity $u - iv$

φ Flow rate coefficient = $\frac{\text{Axial velocity}}{\text{Tip speed}}$

$\bar{\varphi}$ Integrated average flow rate coefficient

Ψ Stream function

ψ Head coefficient = Local head rise of pump / $\frac{1}{2}g u_o^2$

$\bar{\psi}$ Integrated average head coefficient

ψ' Theoretical head coefficient with no losses

$\bar{\psi}'$ Work coefficient $\bar{\psi}/E$

Subscripts

∞ Mean value

o Value at the rotor blade tip

1 Value near rotor blade tip on the pressure side of the blade

2 Value near rotor blade tip on the suction side of the blade

t Value in tip clearance

δ_t Based on tip clearance dimension

w Water machine

a Air machine

APPENDIX B

CALCULATION OF $K = \frac{P_\infty - P_v}{\frac{1}{2}\rho W_\infty^2}$ AND ANGLES OF ATTACK

(a.) P_∞ was calculated from the reading of the manometer connected to a piezometer tap in the case of the pump. Corrections were made for the height of the manometer above the tap and for atmospheric pressure.

(b.) P_v was obtained from the steam tables [24] for the measured water temperature.

(c.) ρ was obtained from the steam tables [24] for the measured value of the water temperature.

(d.) W_∞ was calculated by using a mean velocity triangle at the pump's outer radius and the theoretical ψ_o' vs φ_o curve for this machine. γ_2 the exit angle from the entrance vanes was assumed to be the theoretical value and independent of flow rate. The value of γ_2 for this machine is 19° and the ψ_o' vs φ_o curve is given by $\psi_o' = 1.3 - 2\varphi_o$. The following formulas apply under the above assumptions:

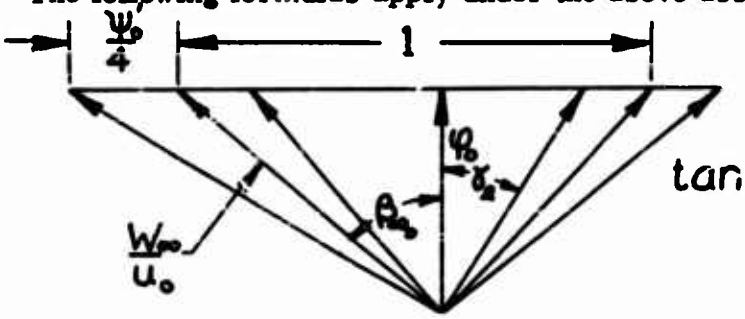

$$\tan\beta_{\infty_o} = \frac{\left(1 - \frac{\psi_o'}{4}\right)}{\varphi_o} - \tan\gamma_2$$

$$\frac{W_{\infty_o}}{u_o} = \frac{\varphi_o}{\cos\beta_{\infty_o}}$$

The angles of attack (α) that are equivalent to certain flow rates were computed from the above results by defining α as $\beta_{\infty_o} - \beta_c^*$, where β_c^* is the stagger angle at the rotor blade tip.

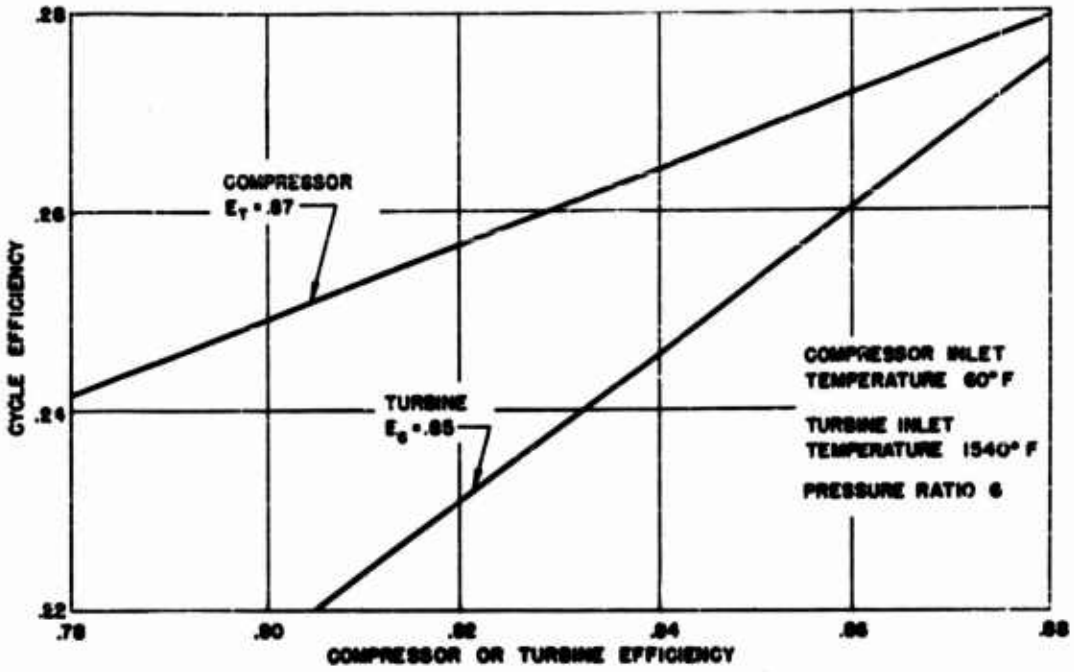

Fig. 1 - Effect of compressor and turbine efficiency on theoretical cycle efficiency.

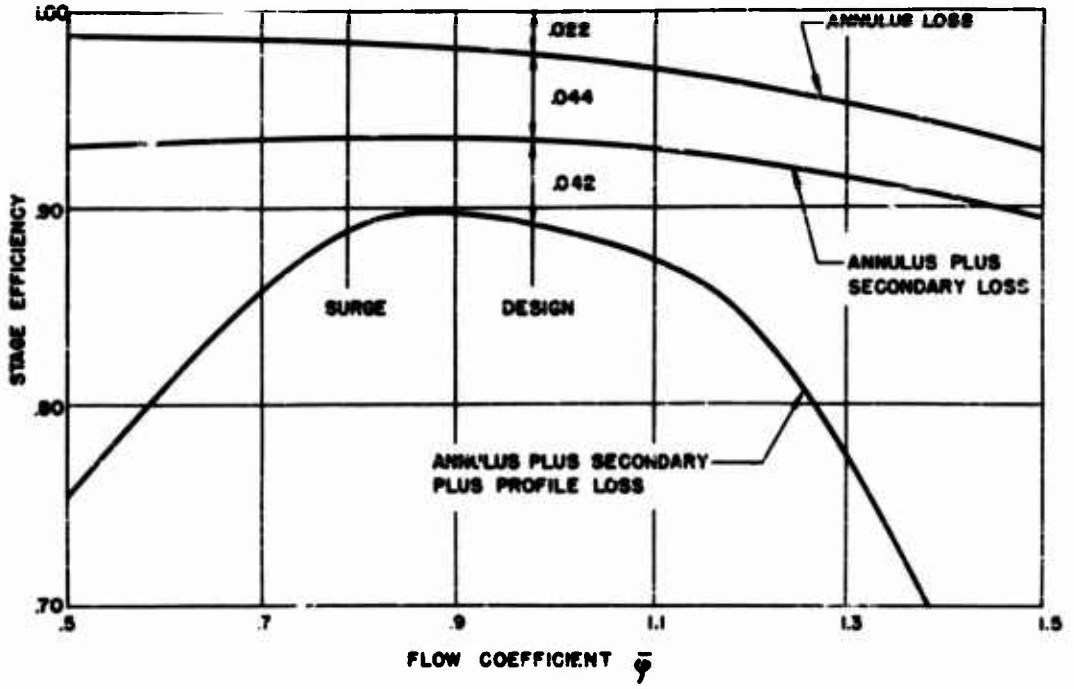

Fig. 2 - An approximate breakdown of the factors affecting compressor efficiency.

Fig. 3 - Test floor of the pump circuit.

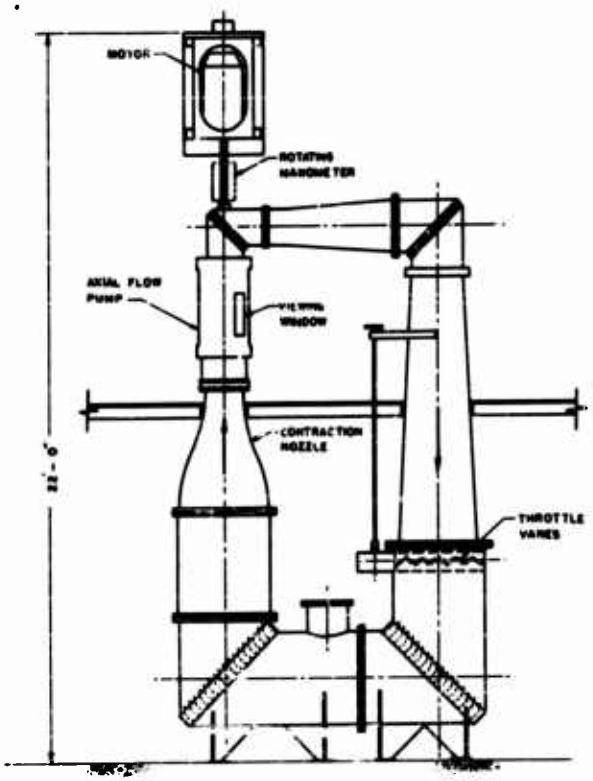

Fig. 4 - Schematic diagram of the pump circuit.

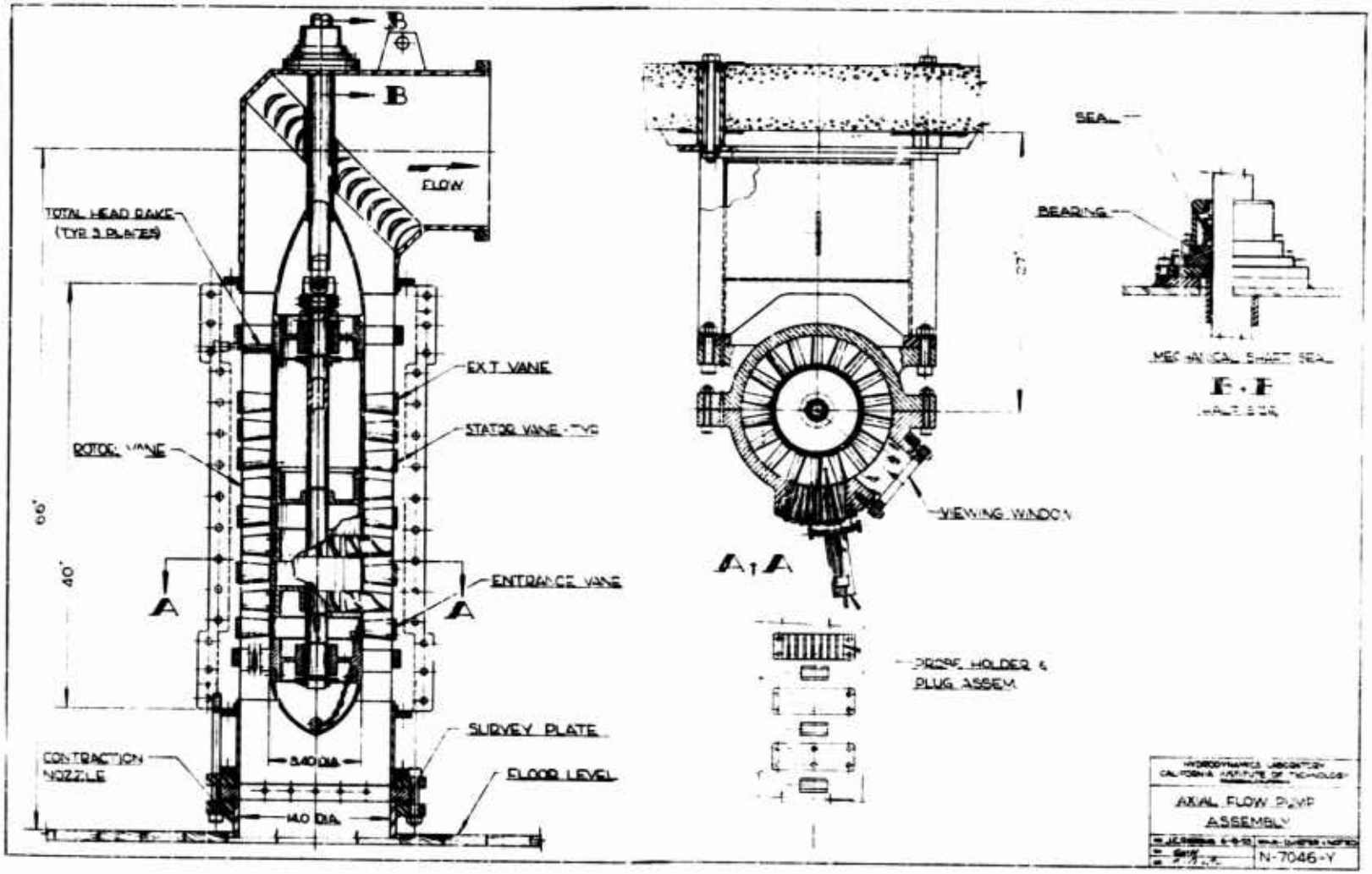

Fig. 5 - Pump test section of the axial flow pump facility.

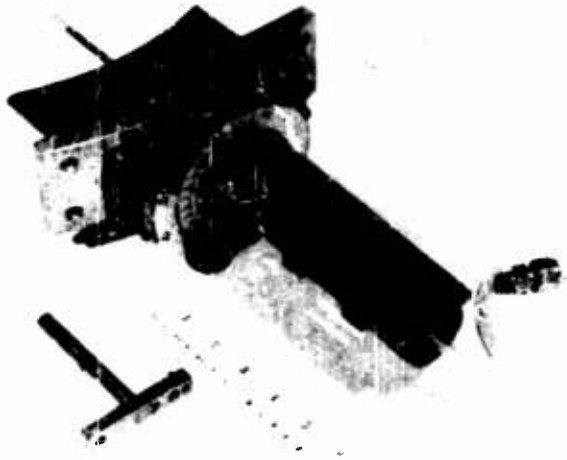

Fig. 6 - Probeholder with probe in place.

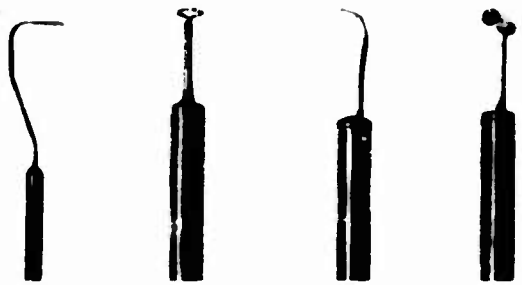

Fig. 7 - Selection of probes.

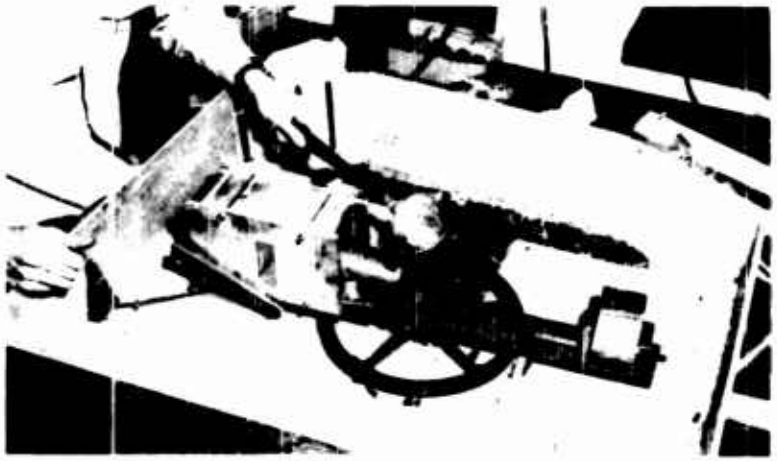

Fig. 8 - Centrifugal casting setup.

Fig. 9 - Rotor blade with variable tip clearance.

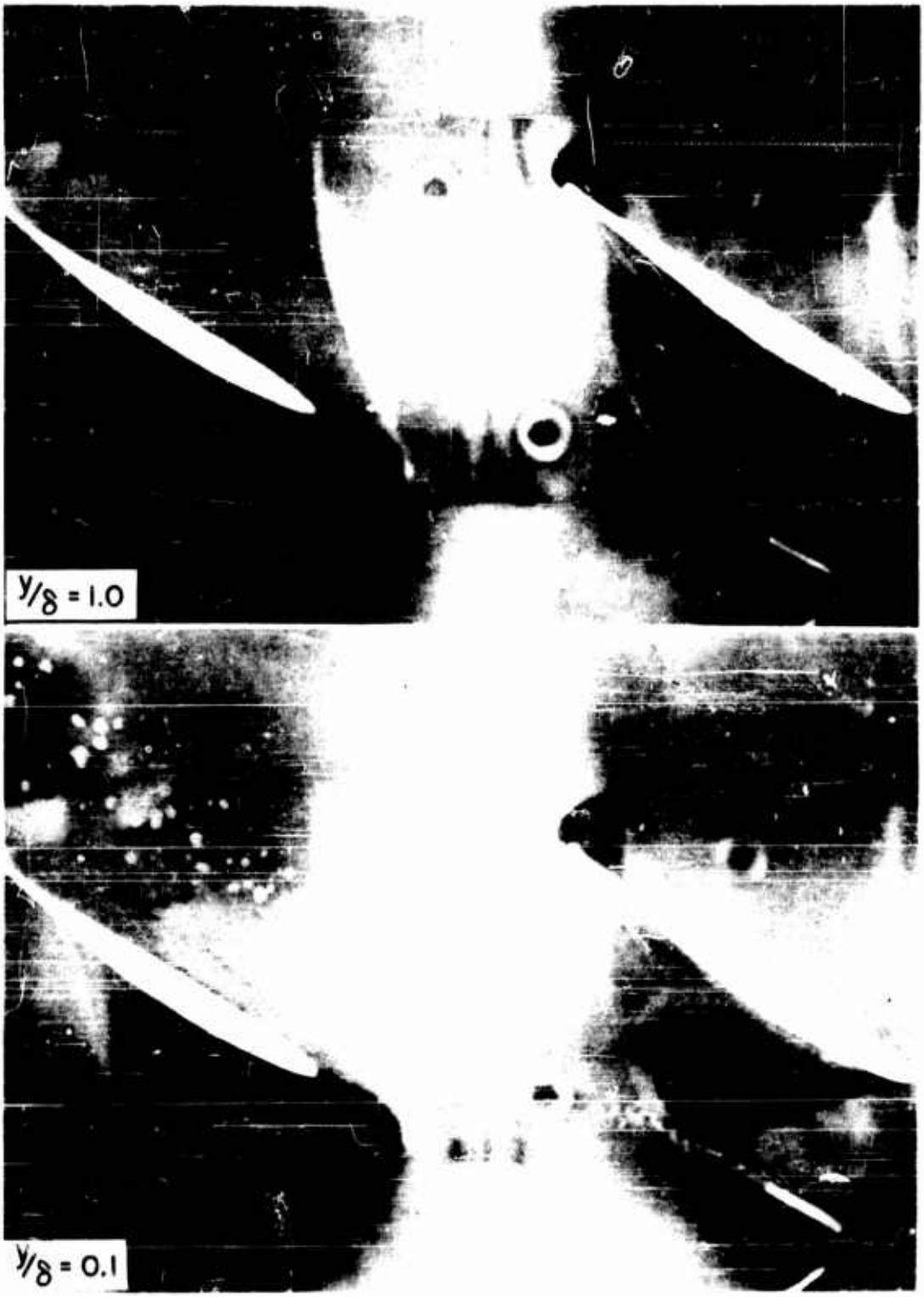

Fig. 10 - Flow visualization technique, illustrating the boundary layer flow at the rotor blade tips.

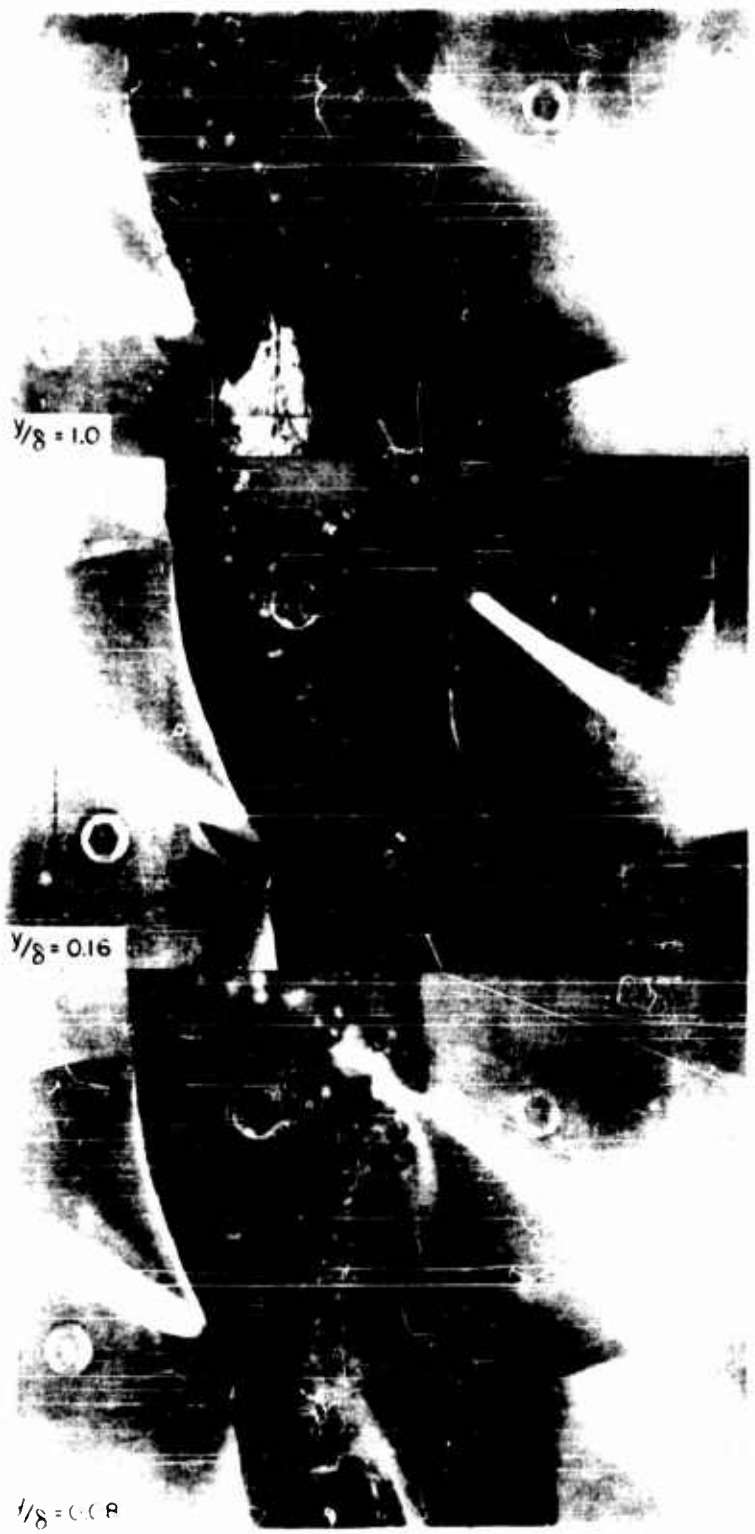

Fig. 11 - Flow visualization of the secondary flows on the rotating hub.

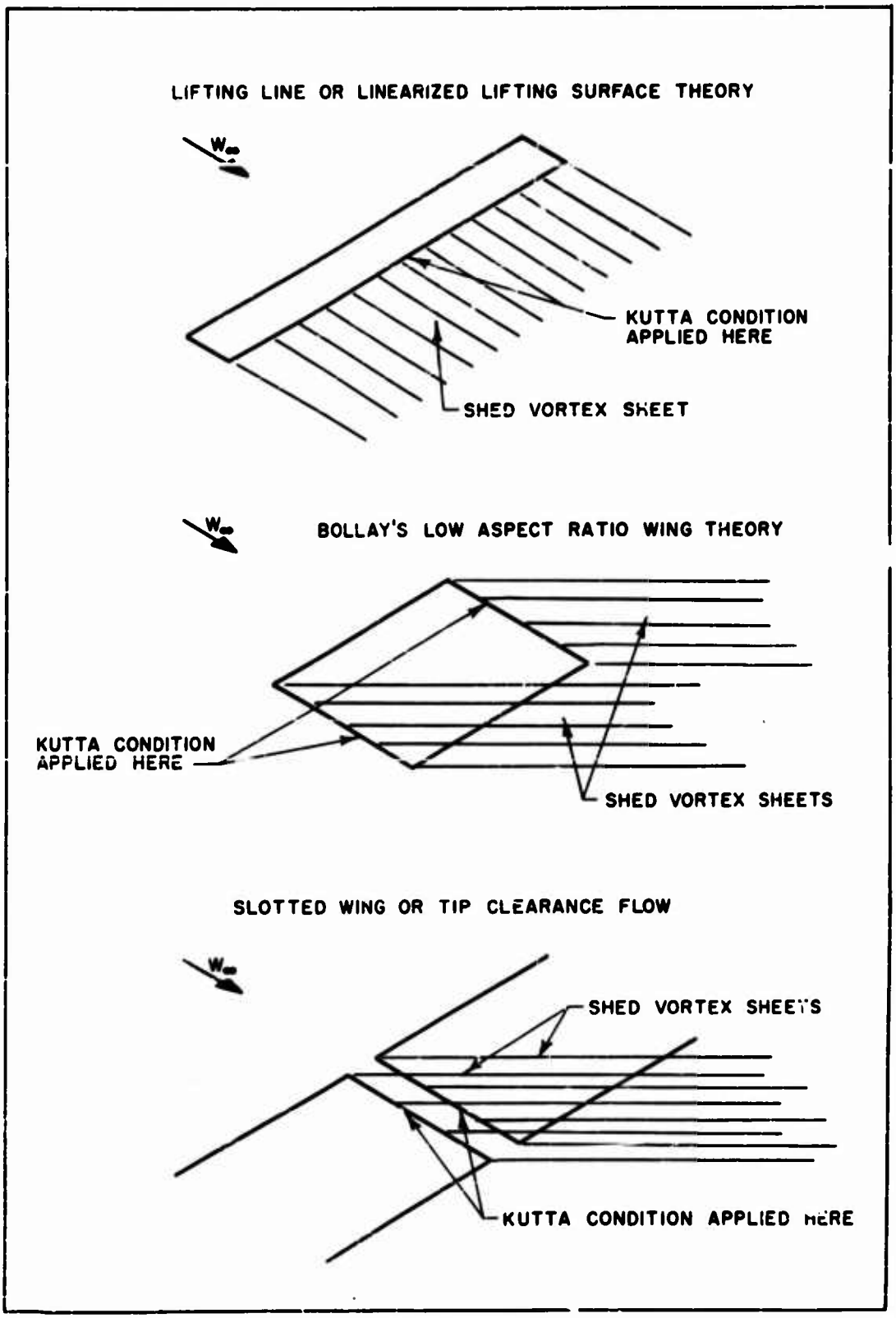

Fig. 12 - Comparison of wing theories and their assumptions on shedding of vorticity.

Fig. 13 - Tip clearance flows for various flow rates.

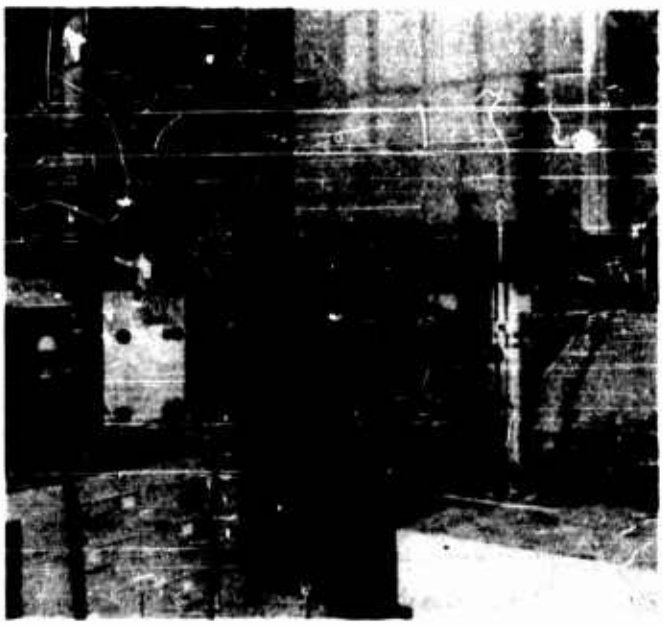

Fig. 14 - Equipment for measuring wall pressure distribution.

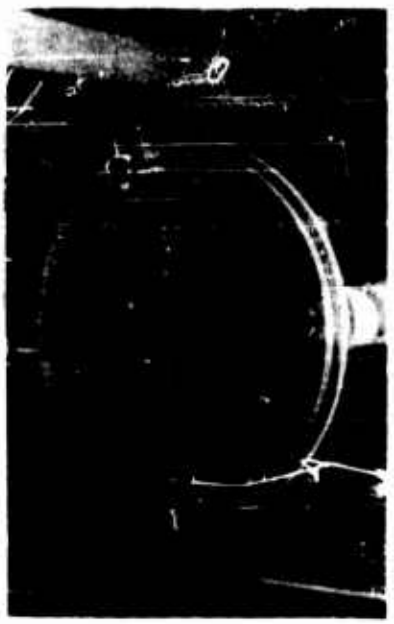

Fig. 15 - Closeup of airfoil and pressure tap disc.

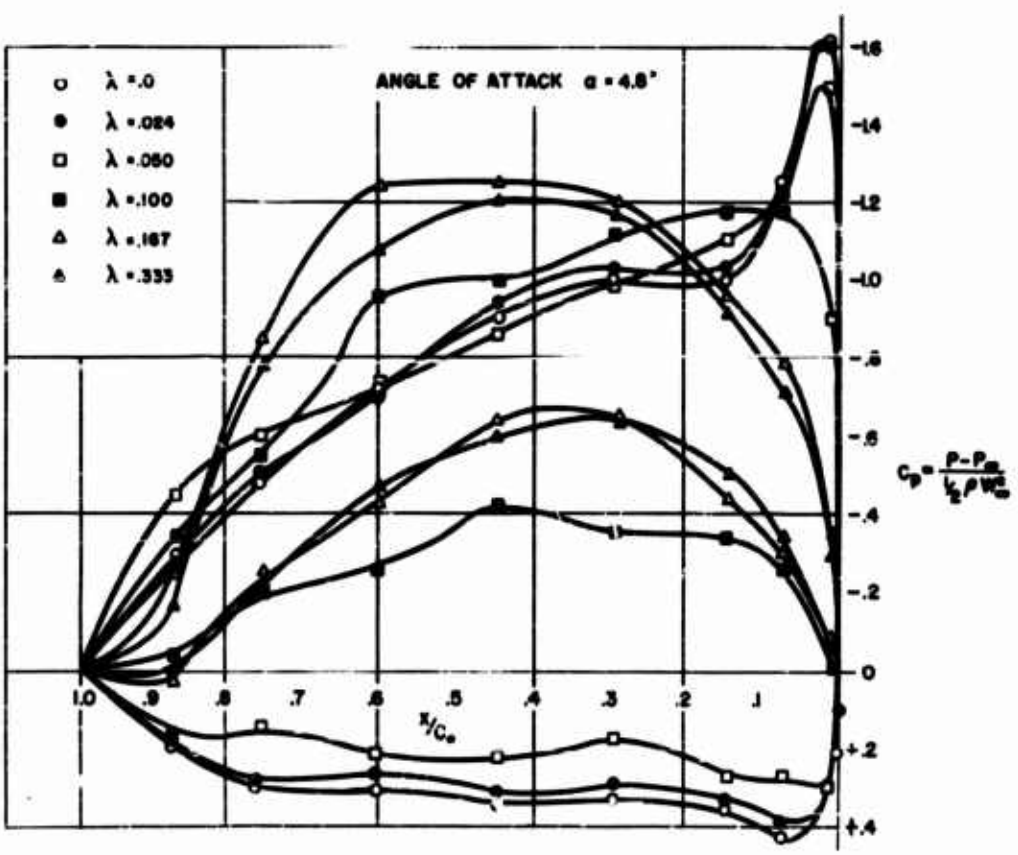

Fig. 16 - Typical wall pressure distribution near the tip of an airfoil.

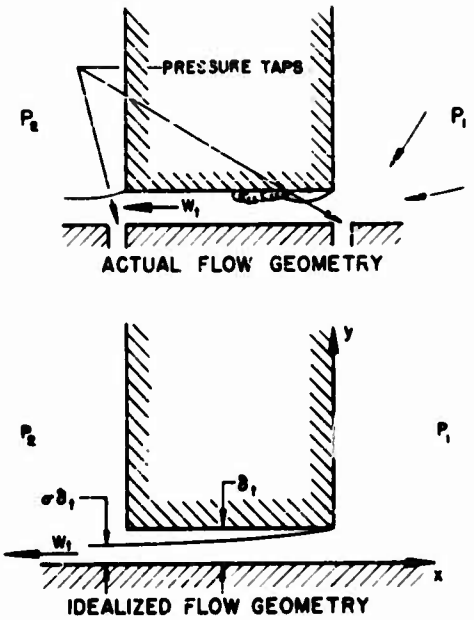

Fig. 17 - Comparison of tip clearance flow geometries.

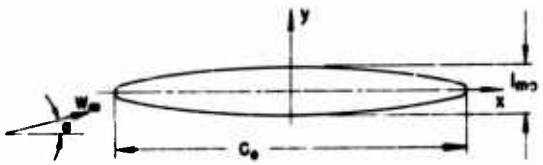

Fig. 18 - Definitions for tip clearance velocity calculations.

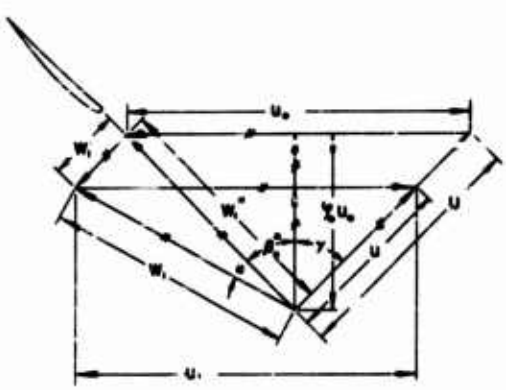

Fig. 19 - Velocity triangle in case boundary layer.

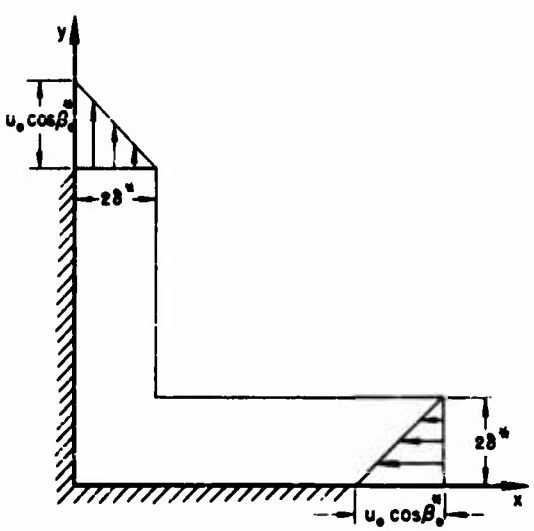

Fig. 20 - Geometry for calculating rotational pressure increase.

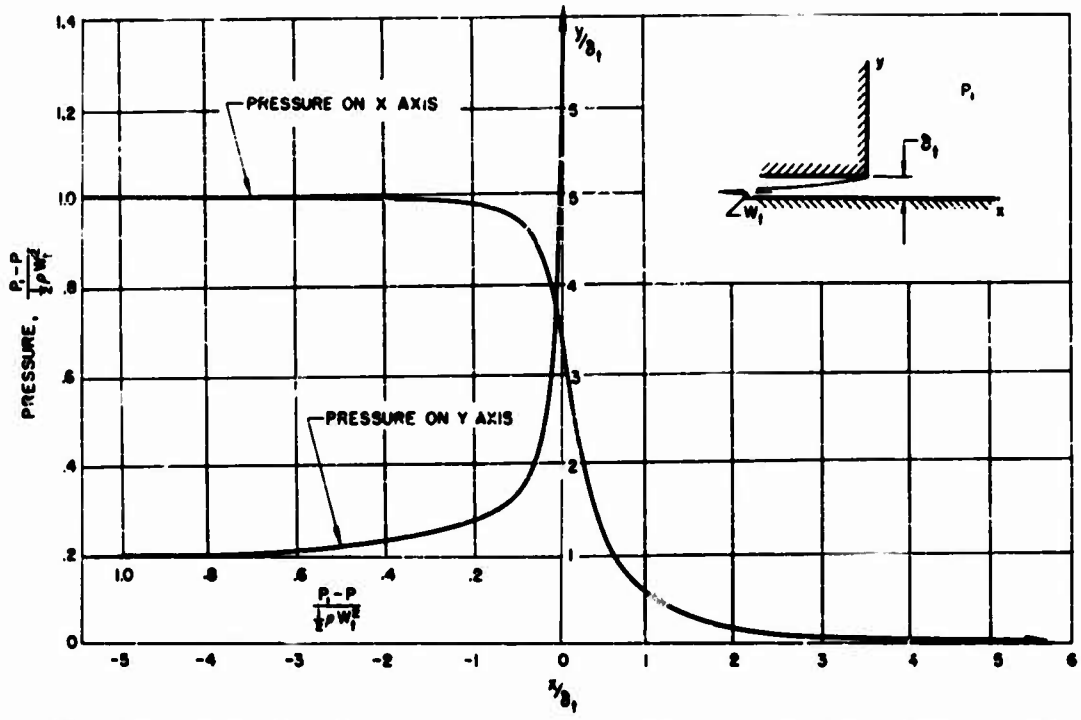

Fig. 21 - Calculated pressures on the walls near the flow into a slot.

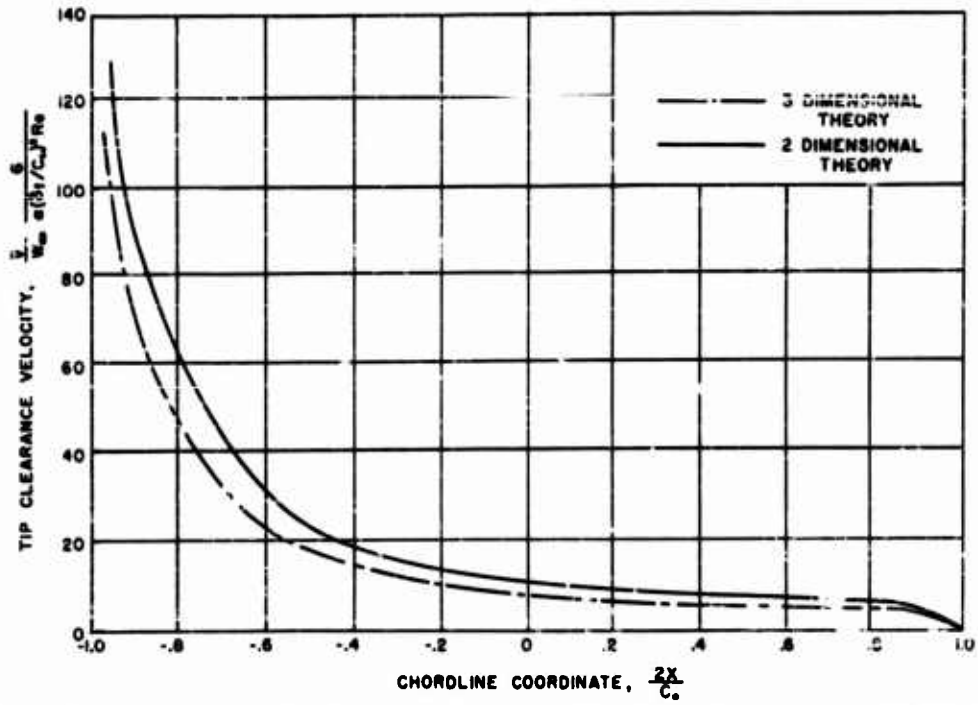

Fig. 22 - Comparison of tip clearance velocities from two- and three-dimensional laminar flow calculations.

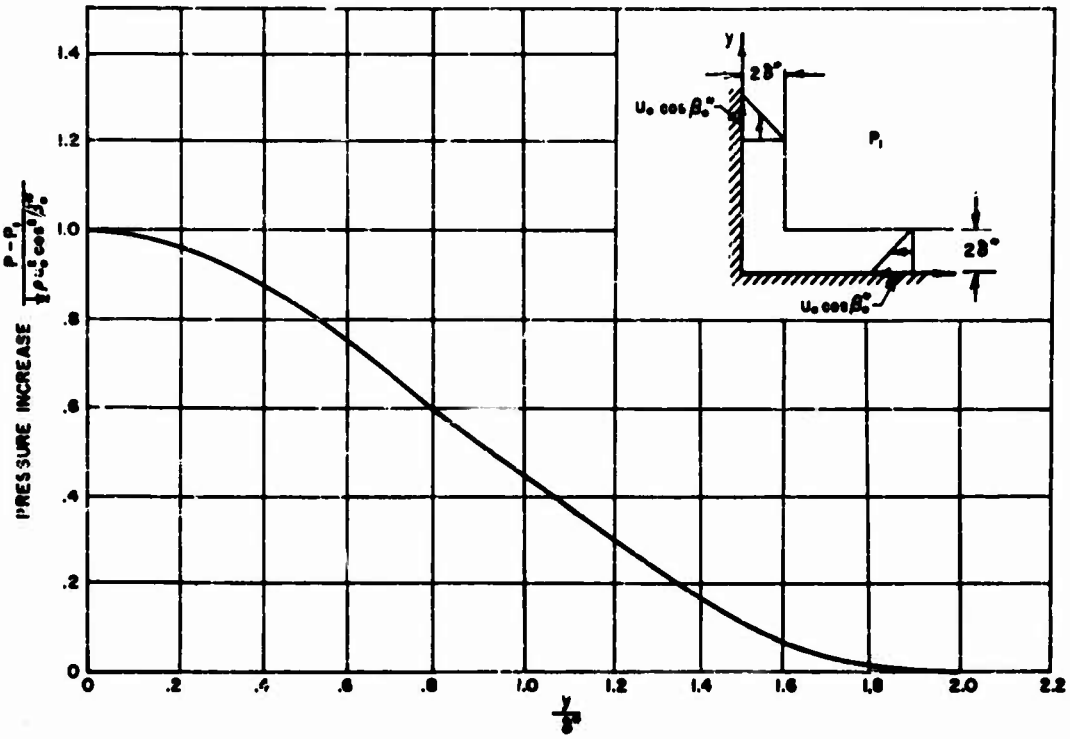

Fig. 23 - Calculated pressure increase at the tip of a rotating blade due to case boundary layer.

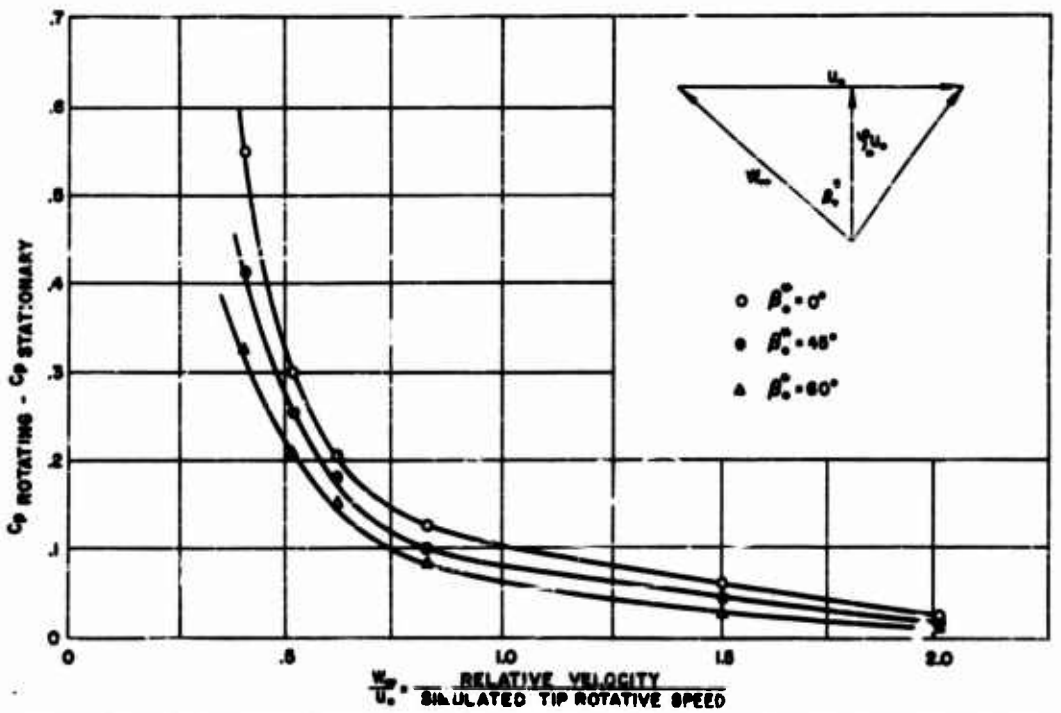

Fig. 24 - Measured pressure increase at the tip of a blade normal to a rotating wall.

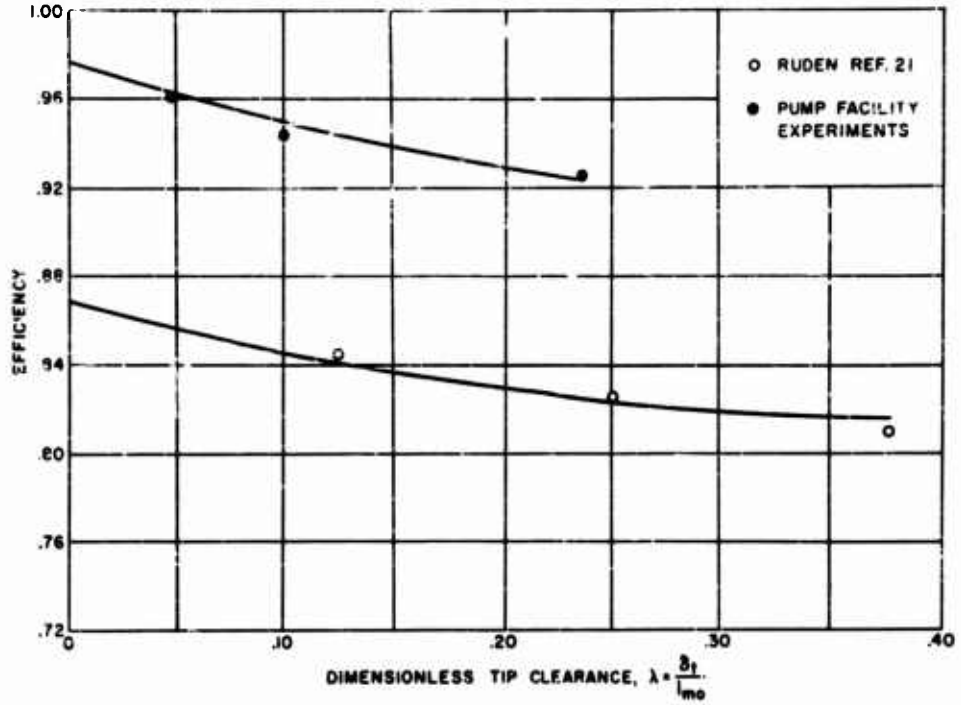

Fig. 25 - Experimental and theoretical variation of the efficiency with rotor tip clearance.

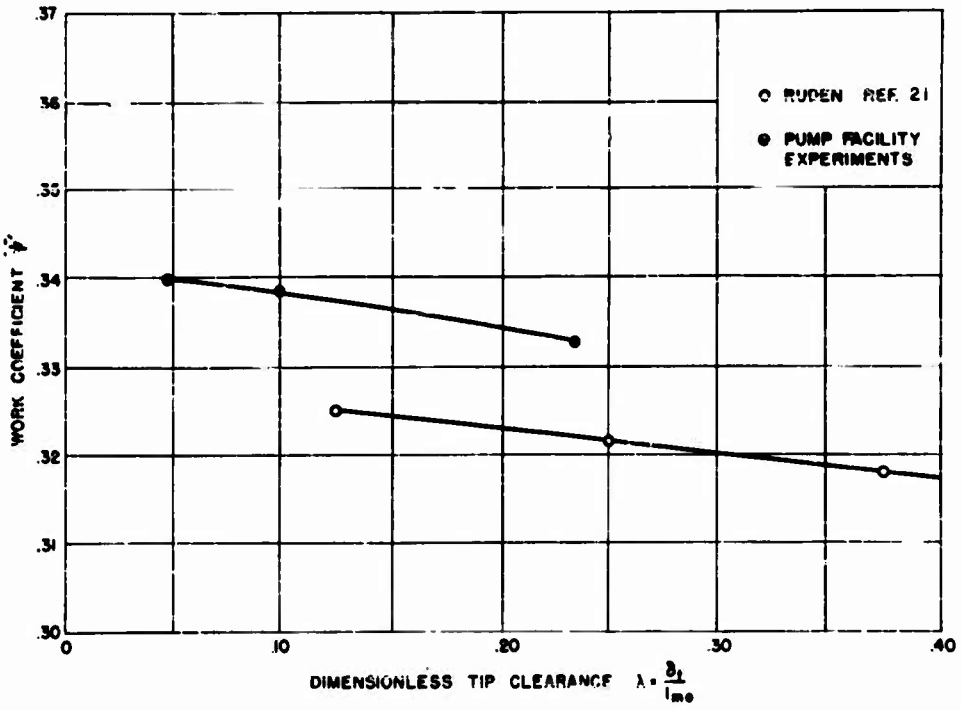

Fig. 26 - Experimentally determined variation of the work coefficient with tip clearance.

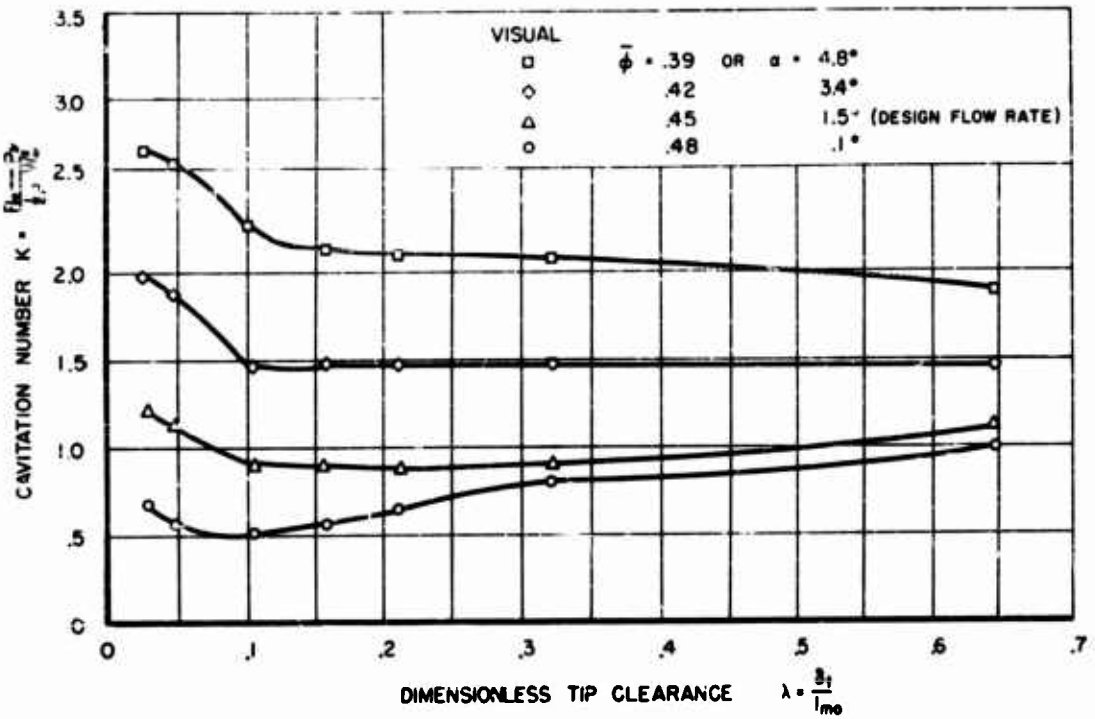

Fig. 27 - Cavitation inception in a pump vs. tip clearance for various flow rates.

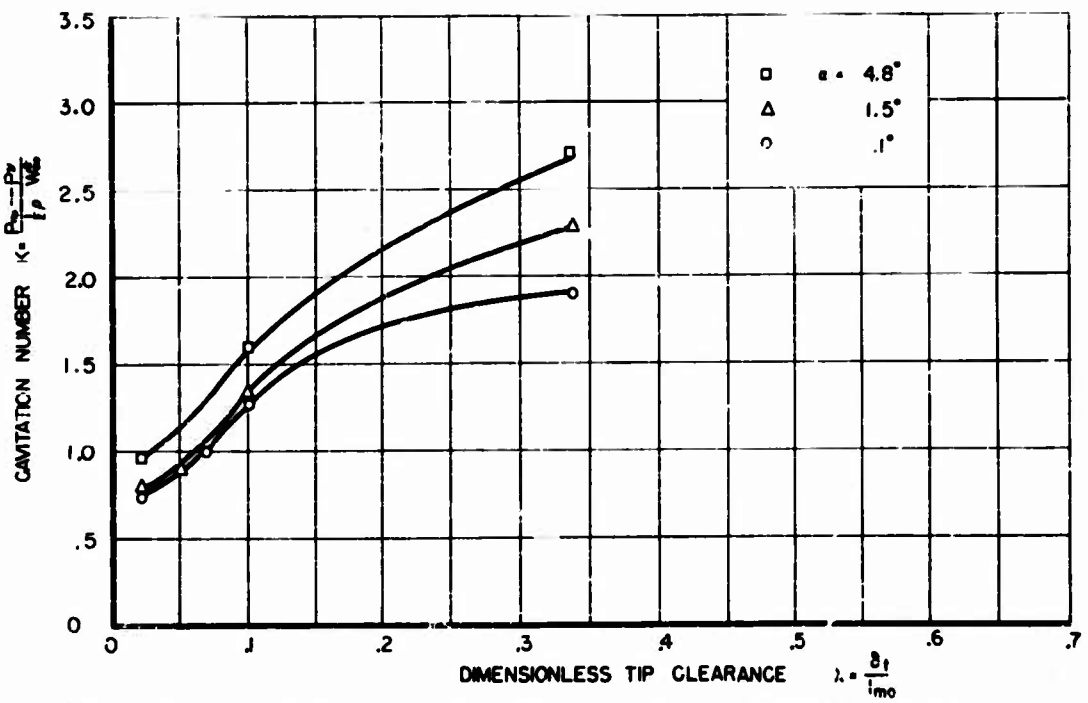

Fig. 28 - Cavitation inception for a single hydrofoil for various angles of attack.

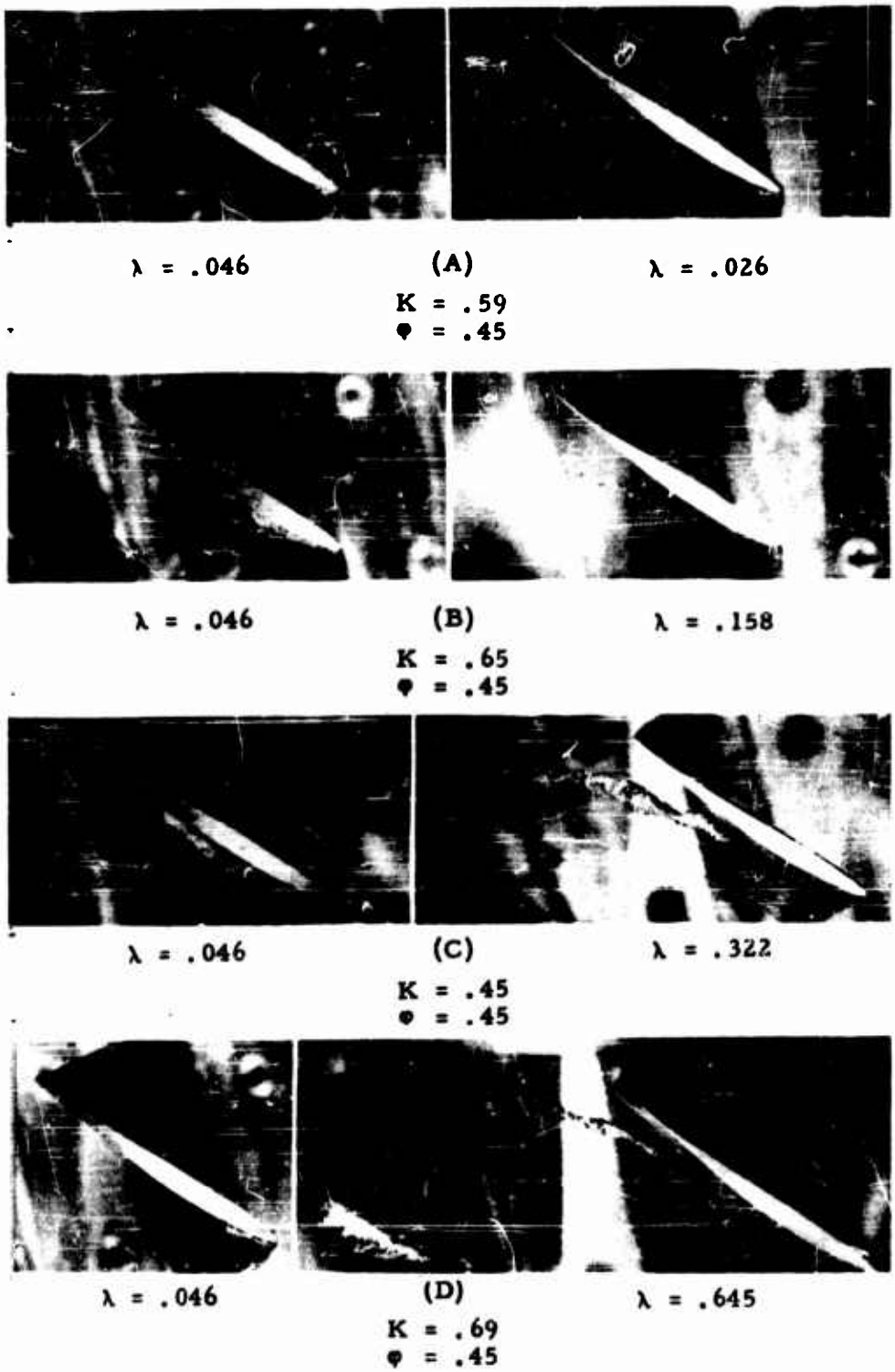

Fig. 29 - A comparison of the vortex structure for various tip clearances.

Fig. 30 - Effect of rounding the pressure side edge of the blade tip on clearance cavitation.

A. $\lambda = .024$ $K = .76$ $\alpha = 4.8^{\circ}$ B. $\lambda = .10$ $K = .69$ $\alpha = .1^{\circ}$

C. $\lambda = .34$ $K = .80$ $\alpha = .1^{\circ}$

Fig. 31 - Clearance vortex cavitation near a single stationary hydrofoil.

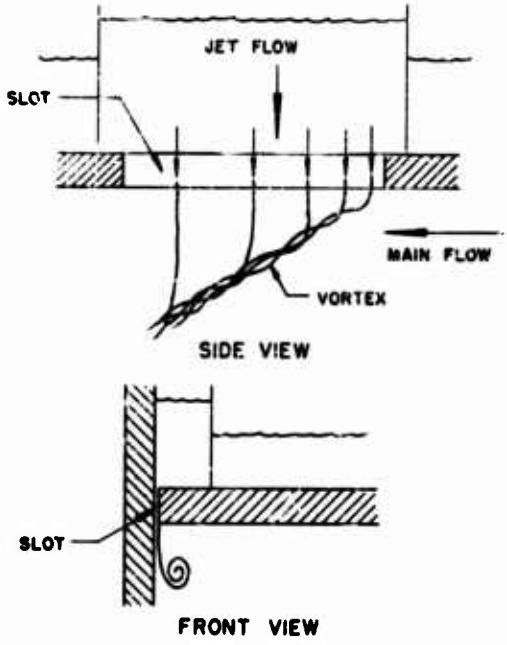

Fig. 32 - Vortex formation visualization experiment.

Fig. 33 - Vortex sheet cavitation in a commercial pump.

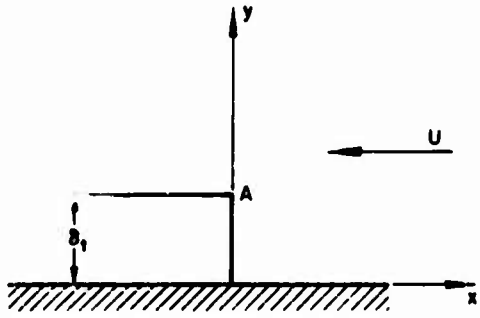

Fig. 34 - Initial conditions for jet roll-up calculations.

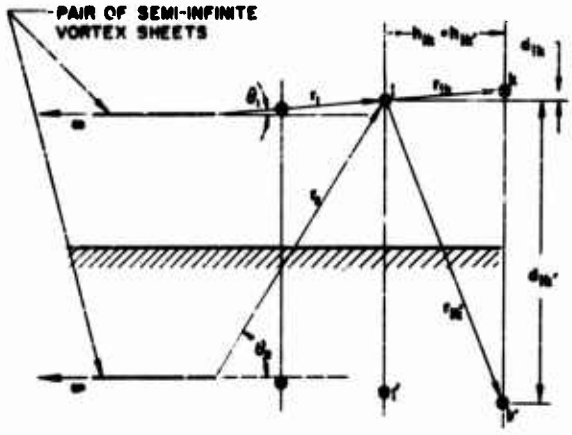

Fig. 35 - Geometric definitions for jet roll-up calculations.

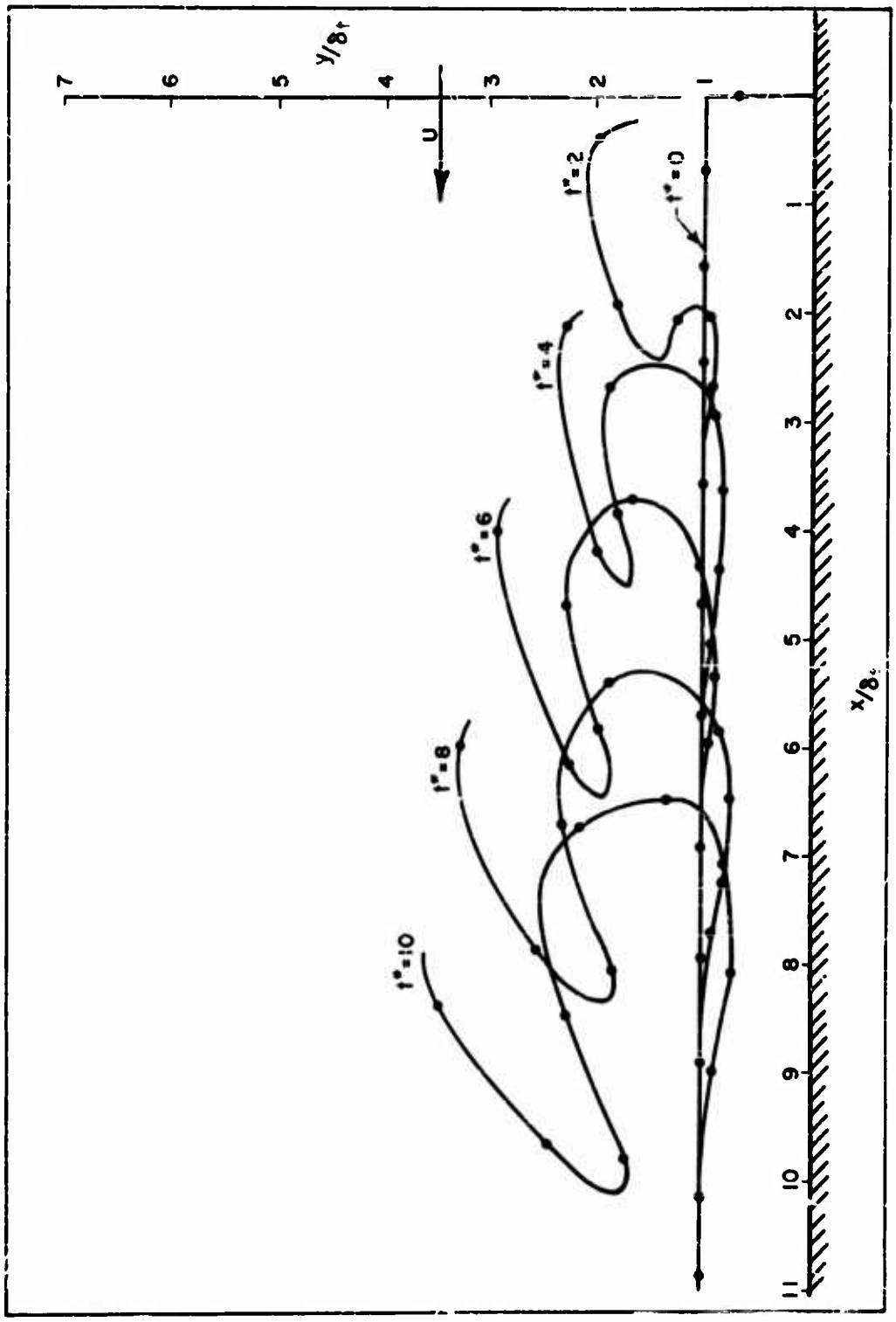

Fig. 36 - The motion of the discontinuity surface between a thin jet and through flow as the jet enters the stream.

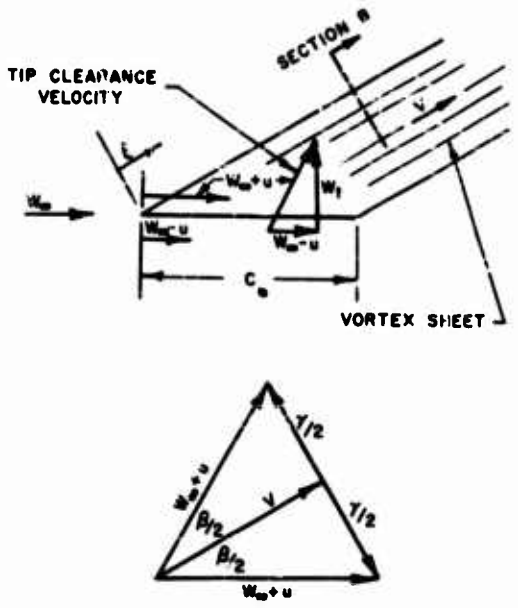

Fig. 37 - Formation of shed vortex sheet from an airfoil.

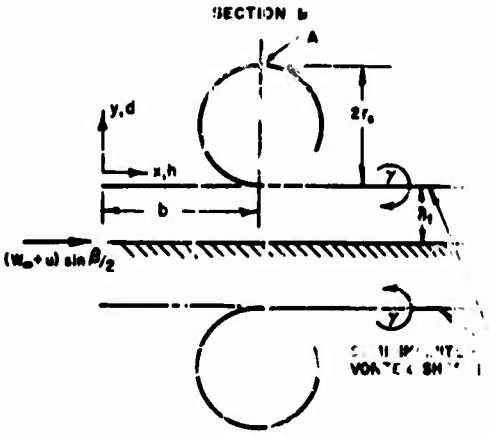

Fig. 38 - Cross-section view of the shed vortex sheet.

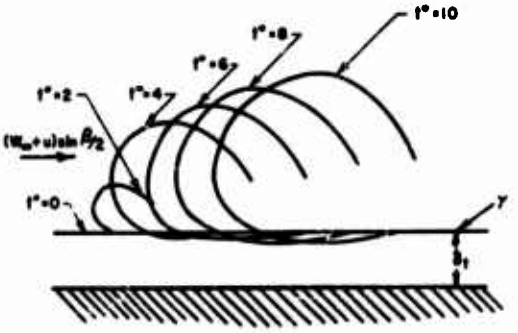

Fig. 39 - Vortex sheet roll-up pattern.

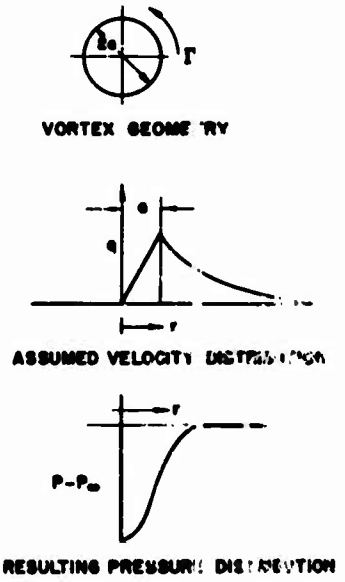

Fig. 40 - Rectilinear vortex description and properties.